Supplement of Earth Syst. Sci. Data, 16, 3601–3685, 2024
https://doi.org/10.5194/essd-16-3601-2024-supplement

Supplement of

State of Wildfires 2023–2024

Matthew W. Jones et al.

Correspondence to: Matthew W. Jones (matthew.w.jones@uea.ac.uk), Douglas I. Kelley (doukel@ceh.ac.uk), Chantelle A. Burton (chantelle.burton@metoffice.gov.uk), and Francesca Di Giuseppe (francesca.digiuseppe@ecmwf.int)

Supplementary Figures

Figures referred to in the main text.

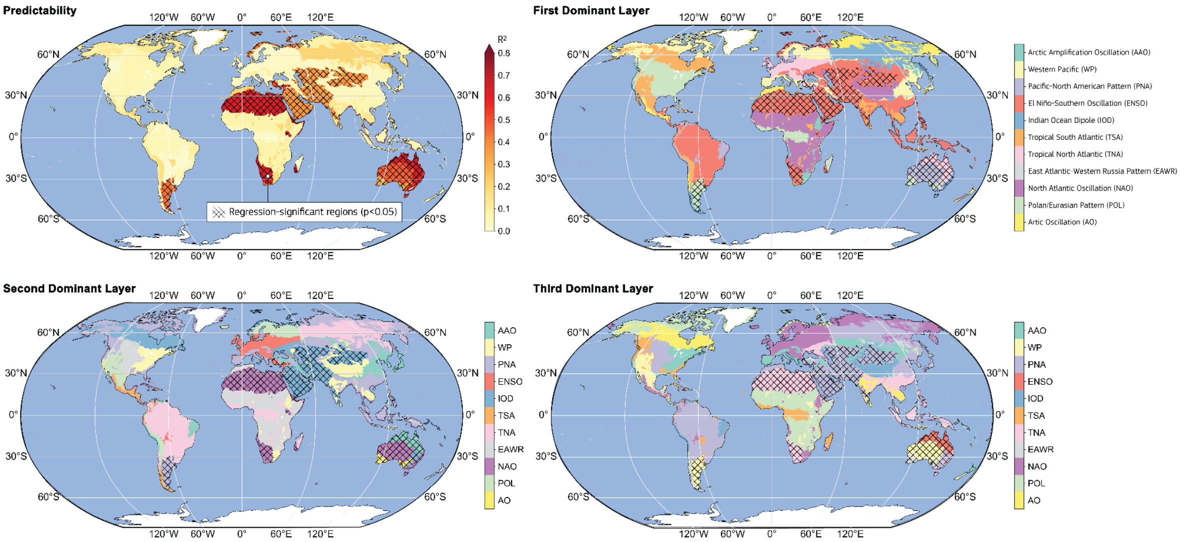

Figure S1: Influence of modes of climate variability on Burned Area (BA) in the period 2001-2020. The figure maps the mode of climate variability with a dominant (and secondary, and tertiary) influence on interannual variability in BA. The coefficient of covariation (R^2) value linking BA to each mode is also shown. The modes included are: Antarctic Oscillation (AAO); West Pacific (WP) pattern; Pacific–North American (PNA) pattern; El Niño–Southern Oscillation (ENSO); Indian Ocean Dipole (IOD); tropical South Atlantic (TSA) pattern; tropical North Atlantic (TNA) pattern; East Atlantic/Western Russia (EAWR) pattern; North Atlantic Oscillation (NAO); Polar-Eurasian (POL) pattern;and the Arctic Oscillation (AO).

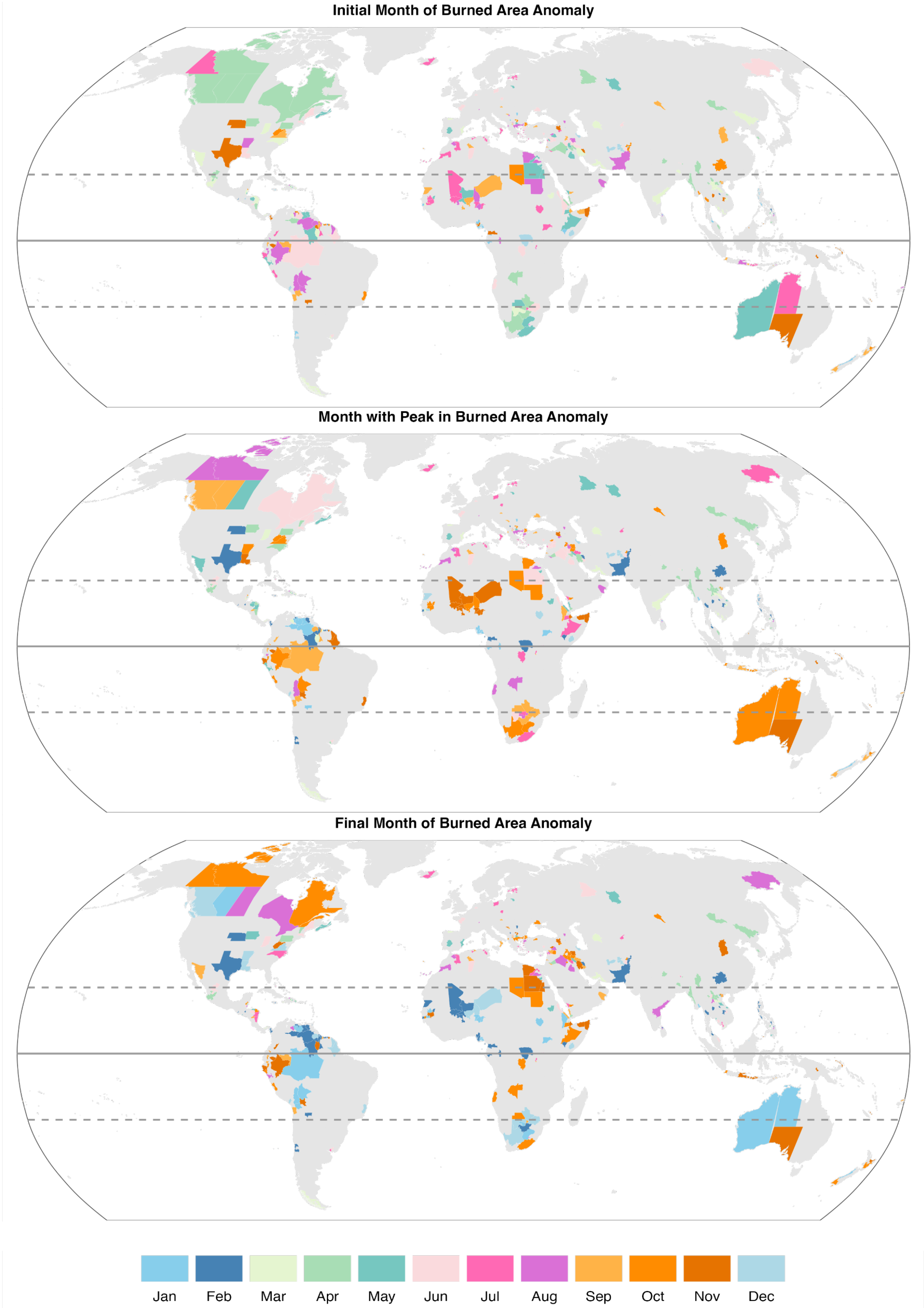

Figure S2: (Top panel) first month, **(middle panel)** peak month, and **(lower panel)** final month of positive BA anomalies at Global Administrative Level 1 during March 2023-February 2024. Peak anomalies are identified relative to the monthly climatology in 2002-2023. The first and final months of the BA anomaly incorporate the period when BA was continuously above the climatological mean. Graduated colours are separated seasonally.

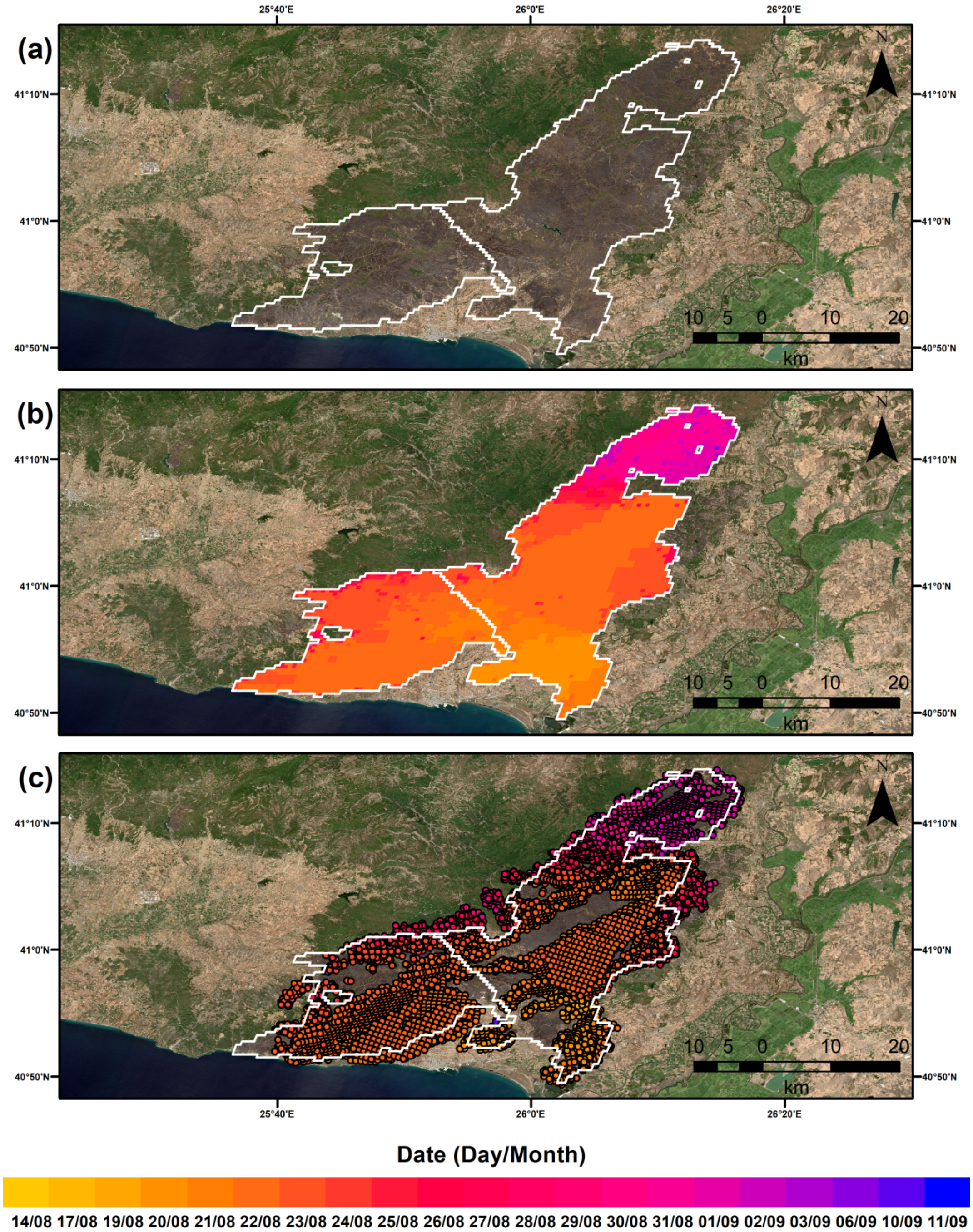

Figure S3: Perimeter and daily progression of the largest fire ever recorded in the EU (Xanthopoulos et al., 2024; EU Science Hub, 2023), near Alexandroupolis in Macedonia and Thrace, Greece. Panel **(a)** shows a Sentinel-2 true colour composite image (10 m resolution) from 12th September 2023, the day after the fire ceased to grow. The darker colour of recently-burned surfaces contrasts with green unburned forests in surrounding areas. Overlaying the image are lines marking the perimeter of the Alexandroupolis fire from the Global Fire Atlas. Panel **(b)** additionally shows the burn date according to the MODIS BA dataset MCD64A1 (500 m resolution), and for comparison panel **(c)** shows the burn date from active fire detections from the Visible Infrared Imaging Radiometer Suite (VIIRS) sensor (375 m resolution; Schroeder et al., 2014).

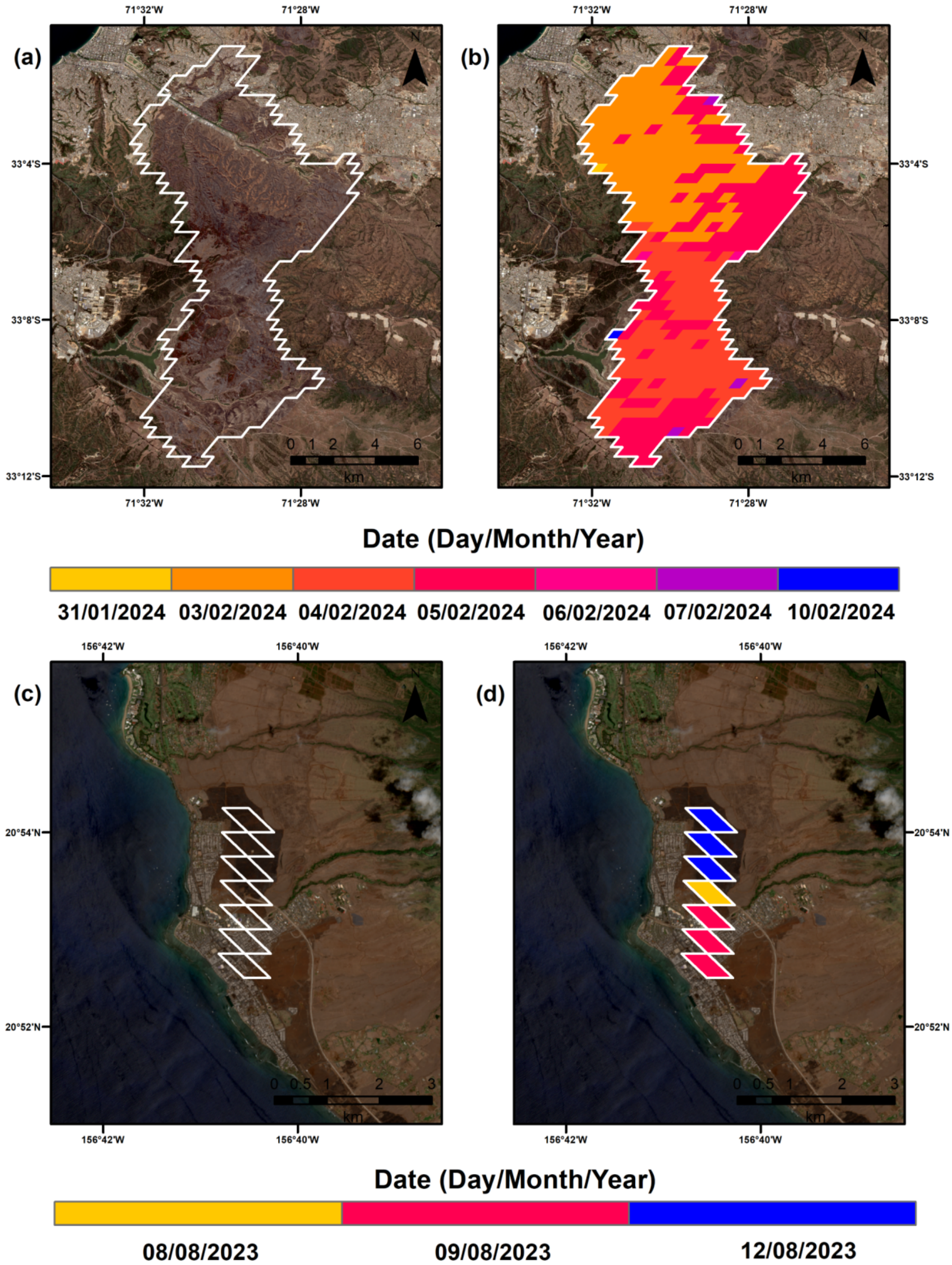

Figure S4: Perimeter and daily progression of extreme individual fires in **(a-b)** Valparaíso, Chile, and **(c-d)** Lahaina, Hawai'i. Panels **(a)** and **(c)** show Sentinel-2 true colour composite images (10 m resolution) from 8th March 2024 and 18th August 2023, on the first cloud-free day after each fire. Overlaying the image are lines marking the perimeter of the impactful fire events from the Global Fire Atlas. Panels **(b)** and **(d)** additionally show the burn date according to the MODIS BA dataset MCD64A1 (500 m resolution).

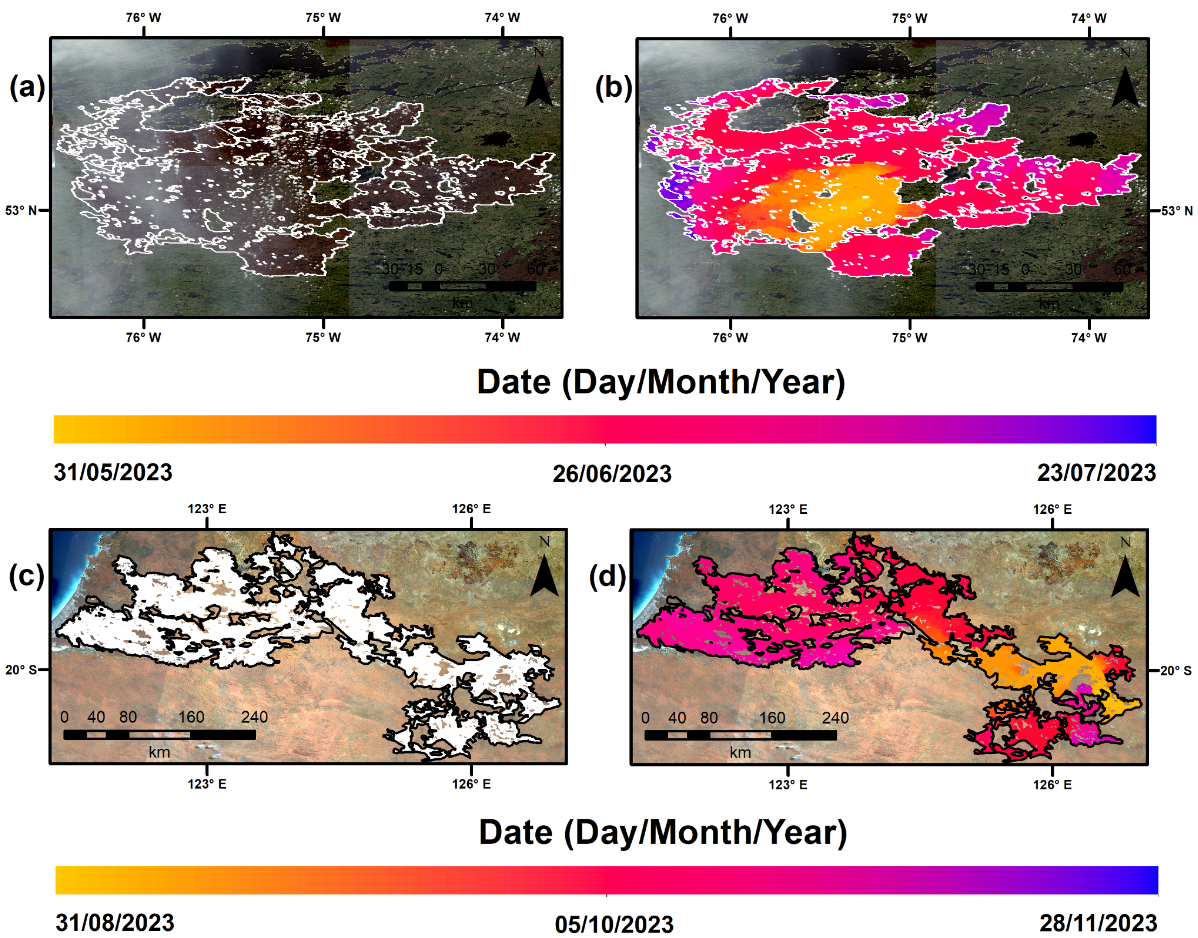

Figure S5: Perimeter and daily progression of extreme individual fires **(a-b)** near La Grande Reservoir in Quebec, Canada, and **(c-d) in the** Great Sandy Desert and Anna Plains, Australia. Panels **(a)** and **(c)** show Sentinel-2 true colour composite images (10 m resolution) based on observations in the periods 25/04/2023-25/08/2023 and 02/09/2023 to 08/09/2023, respectively. Overlaying the image **(a)** are white lines marking the perimeter of the La Grande fire according to the Global Fire Atlas. Overlaying the image **(c)** are white areas marking the area burned by the La Grande fire according to the Global Fire Atlas, and black lines marking the wildfire perimeter from the Department of Fire and Emergency Services in Western Australia. Panels **(b)** and **(d)** additionally show the burn date according to the MODIS BA dataset MCD64A1 (500 m resolution).

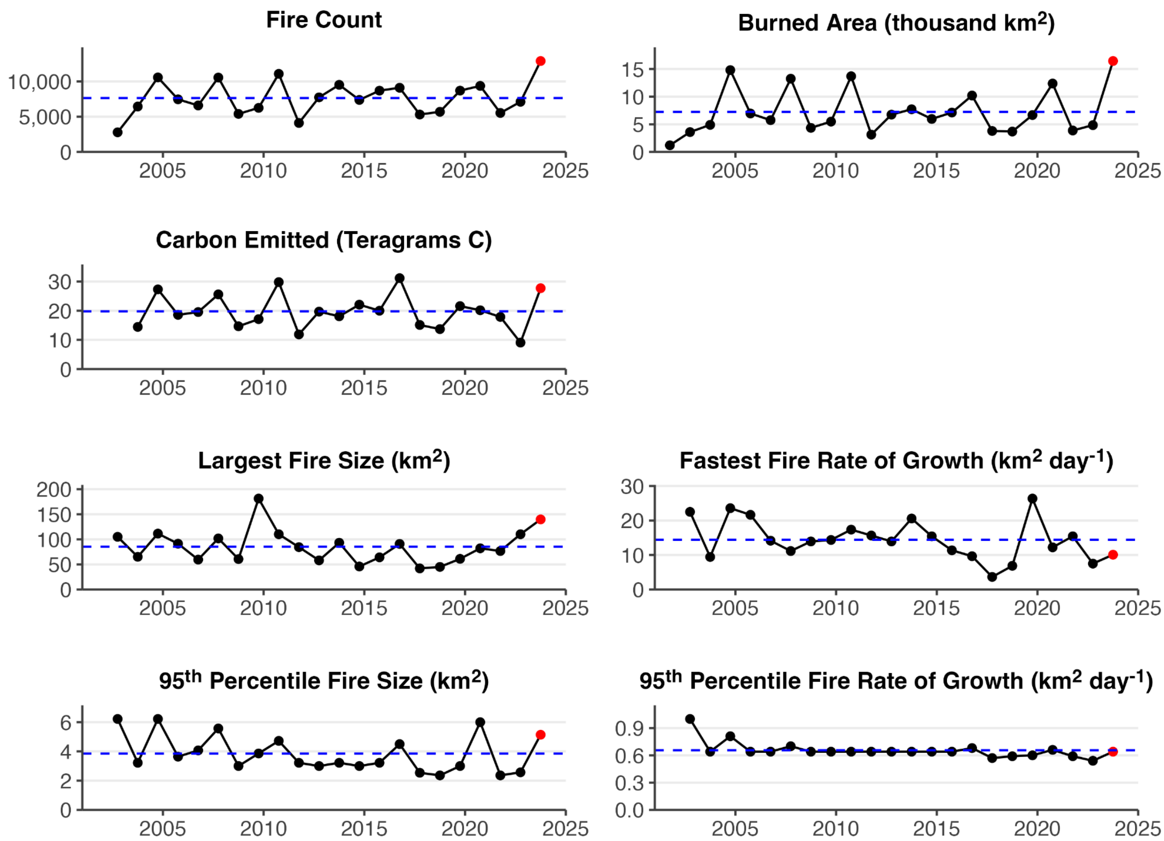

Figure S6: Summary of the 2023-2024 fire season in Lao PDR. Time series of annual fire count, BA, C emissions, PM2.5 emissions, 95th percentile fire size, fastest daily rate of growth, and 95th percentile fire daily rate of growth. Black dots show annual values prior to the latest fire season, red dots the values during the latest fire season, and blue dashed lines the average values across all fire seasons.

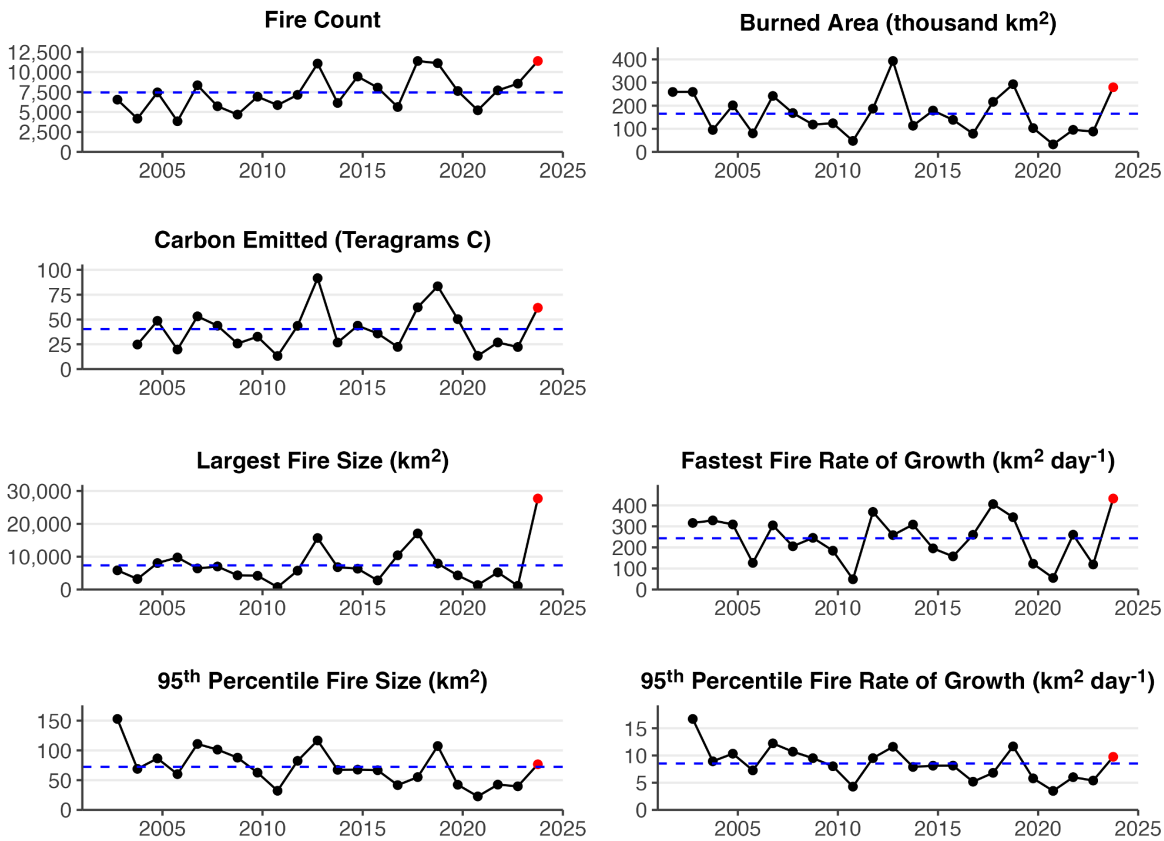

Figure S7: Summary of the 2023-2024 fire season in the state of Western Australia. Time series of annual fire count, BA, C emissions, PM2.5 emissions, 95th percentile fire size, fastest daily rate of growth, and 95th percentile fire daily rate of growth. Black dots show annual values prior to the latest fire season, red dots the values during the latest fire season, and blue dashed lines the average values across all fire seasons.

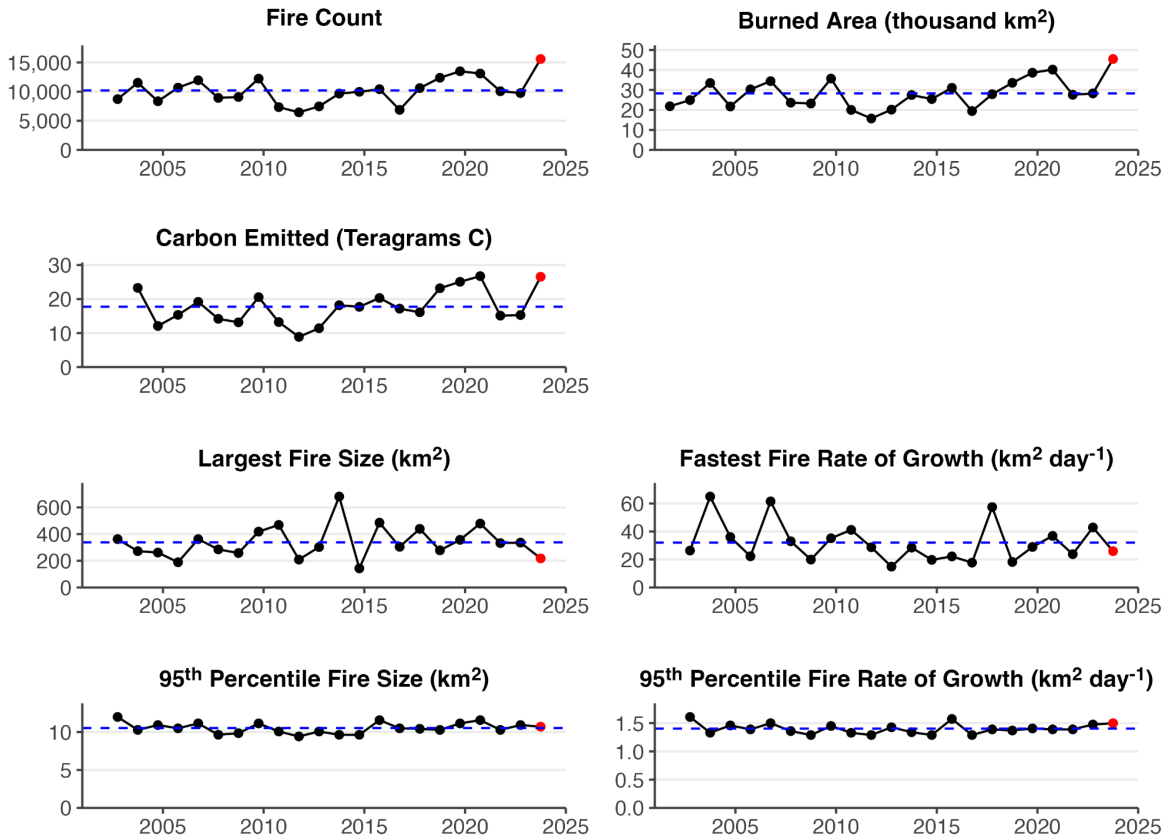

Figure S8: Summary of the 2023-2024 fire season in Venezuela. Time series of annual fire count, BA, C emissions, PM2.5 emissions, 95th percentile fire size, fastest daily rate of growth, and 95th percentile fire daily rate of growth. Black dots show annual values prior to the latest fire season, red dots the values during the latest fire season, and blue dashed lines the average values across all fire seasons.

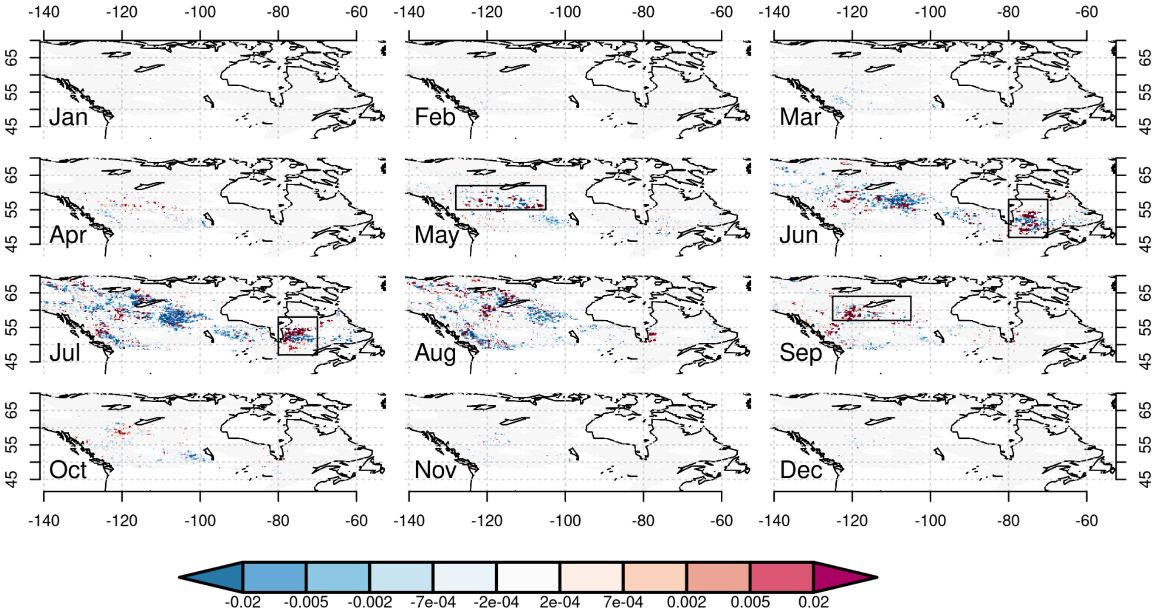

Figure S9: Monthly BA fraction anomaly at 0.25° for Canada for 2023 compare 2002-2023 climatological average. Boxes indicate focal months and regions in driver attribution (**Section 3**).

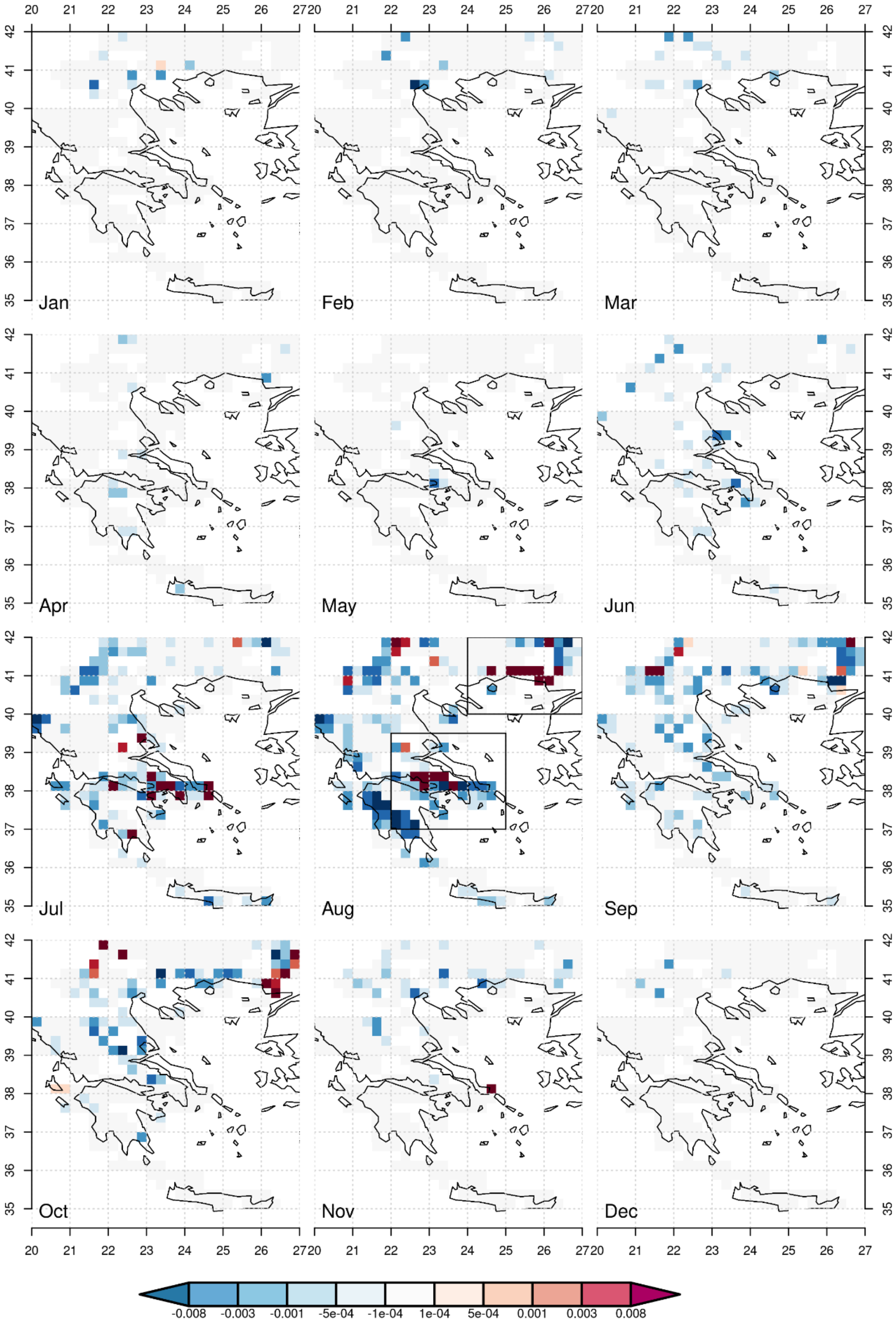

82
83 **Figure S10:** Same as **Figure S9** for Greece

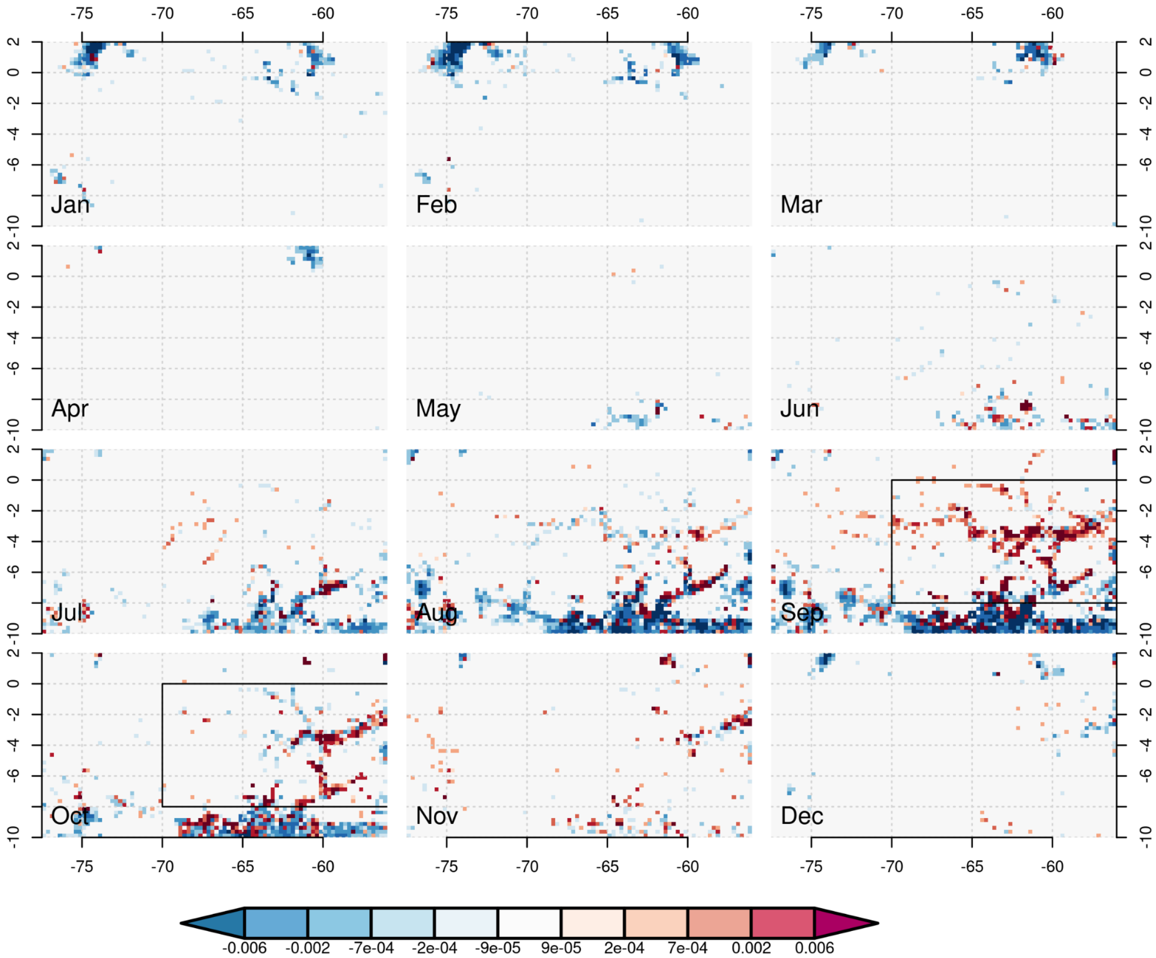

Figure S11: Same as **Figure S9** for Western Amazonia

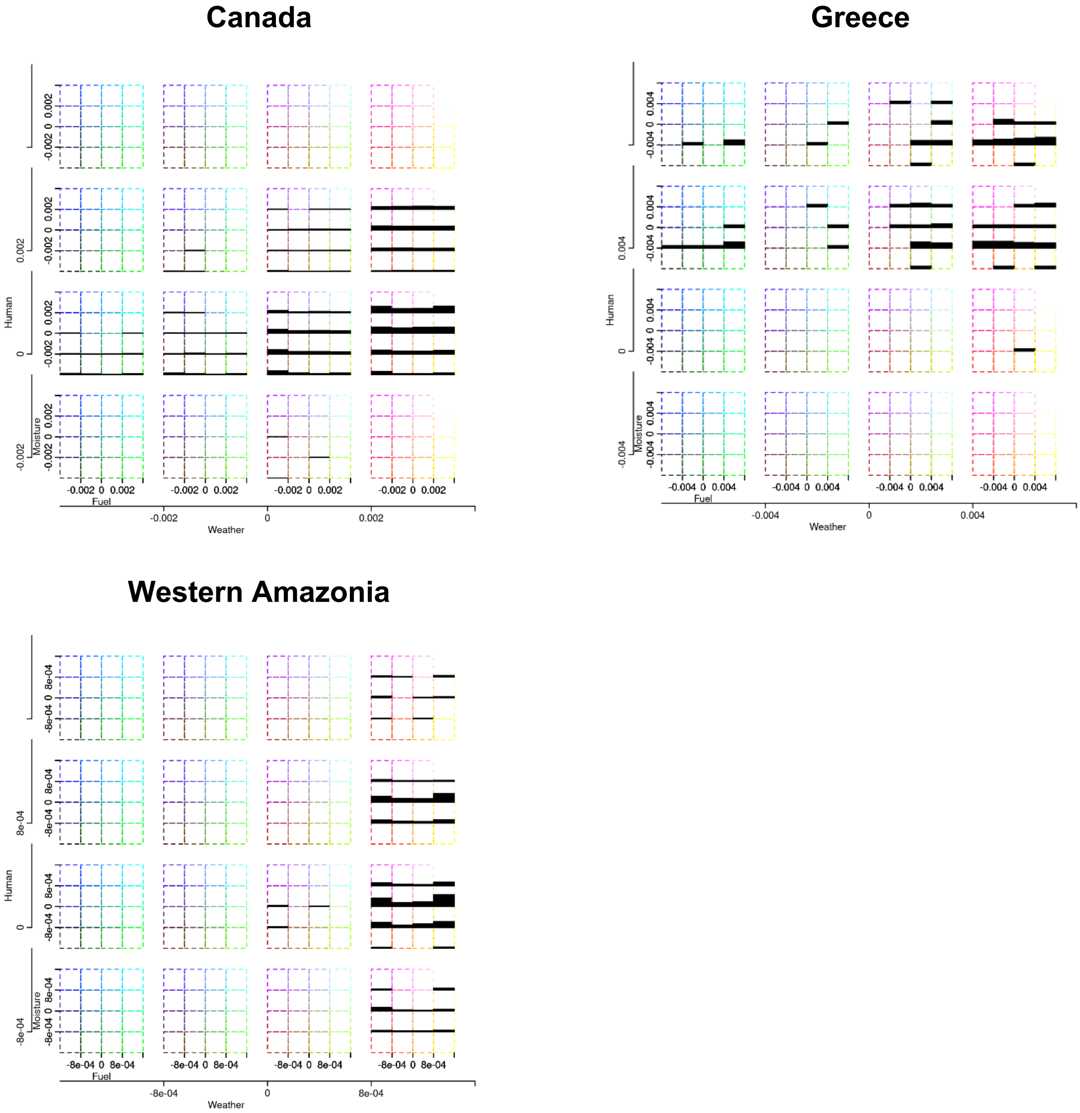

Figure S12: shows the co-occurrence of anomalies for 2023 of our four controls in different regions. In each box of 16 bins, the bottom left corresponds to the negative influence of fuel and moisture on fire anomalies, the top is the positive influence of fuel moisture, and the right indicates a positive influence of fuel load. The bottom left box indicates the negative influence of fire weather and humans, while the right boxes indicate the positive influence of fire weather, and the top indicates the positive influence of humans. The shading of each bin for each region indicates how much of that region falls into that bin. The shades themselves represent the uncertainty range, with grey indicating the 10th percentile and black indicating the 90th percentile.

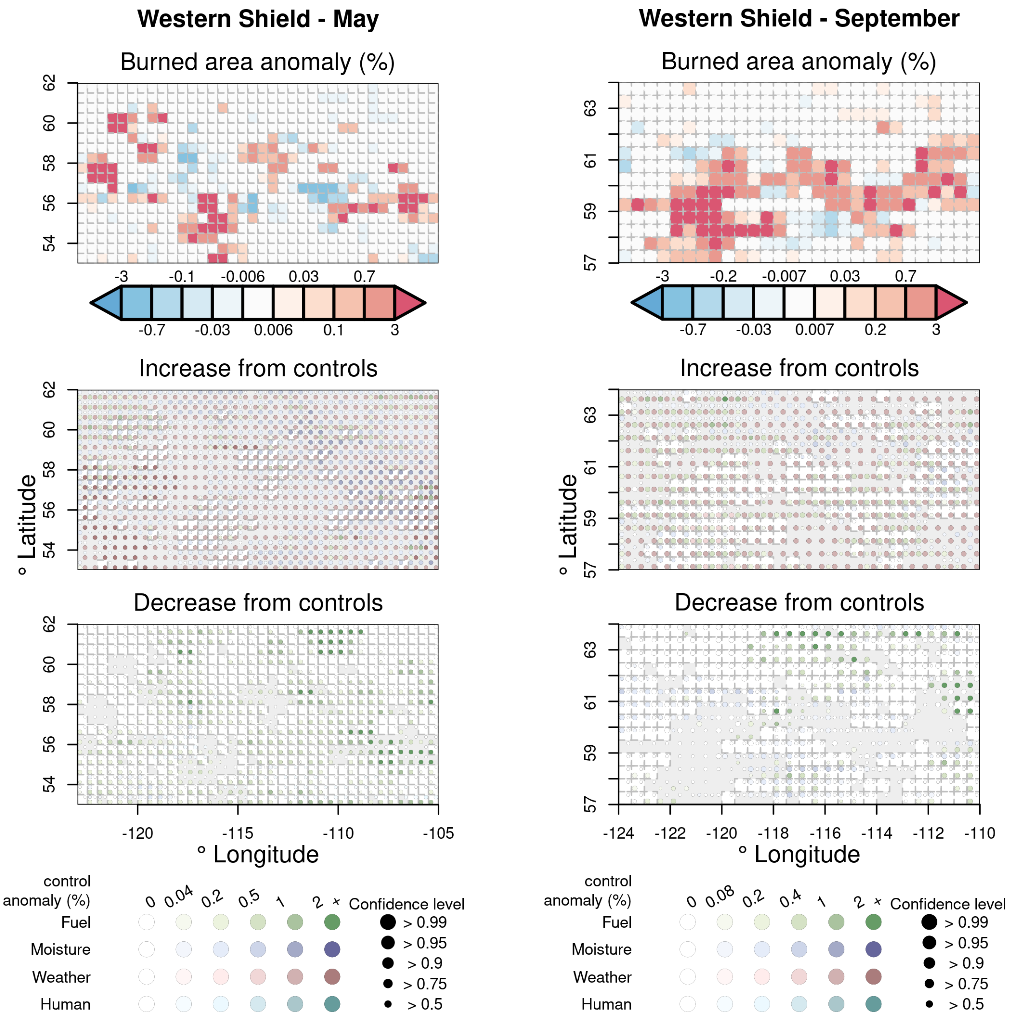

Figure S13: Same as **Figure 11** but for the Canadian Western Shield.

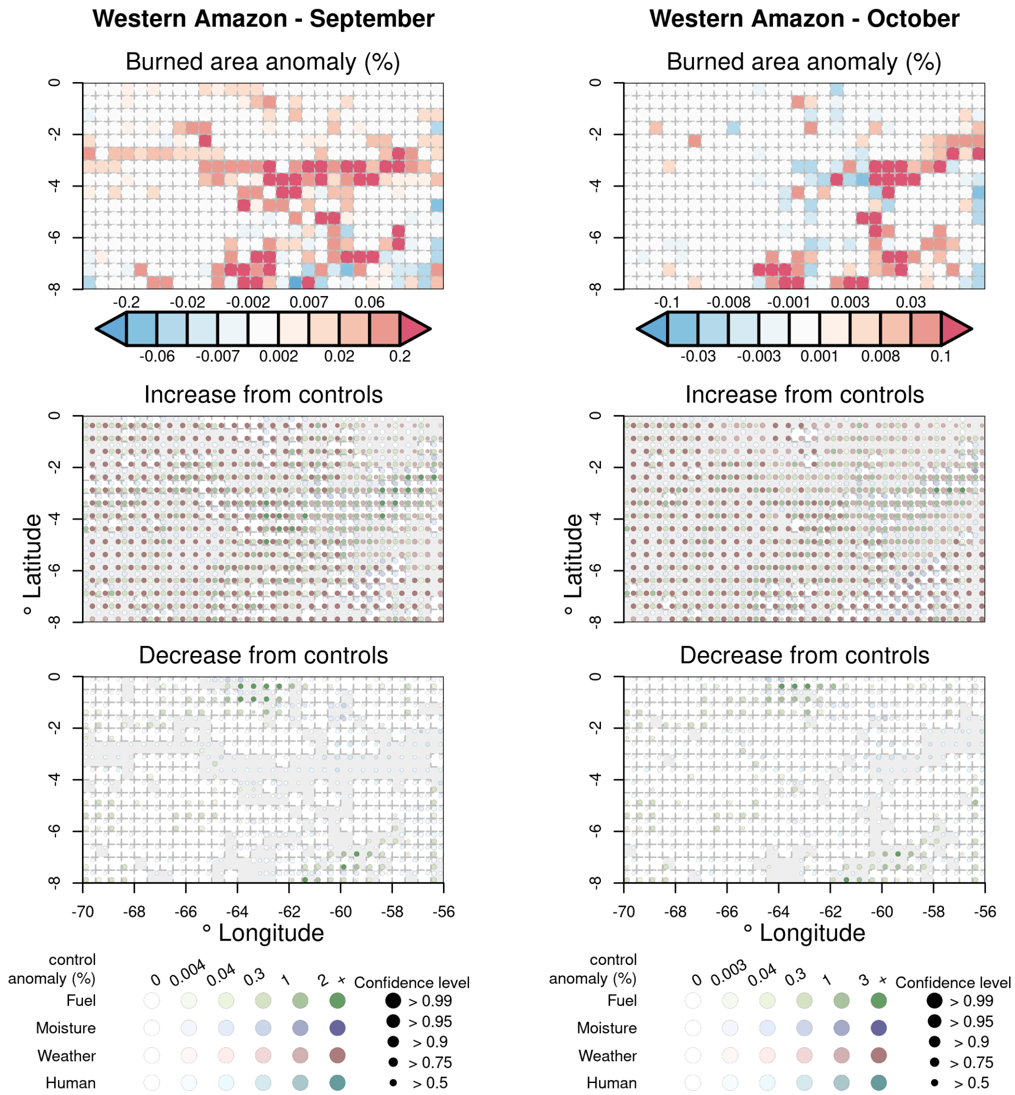

Figure S14: Same as **Figure 11** but for Western Amazonia.

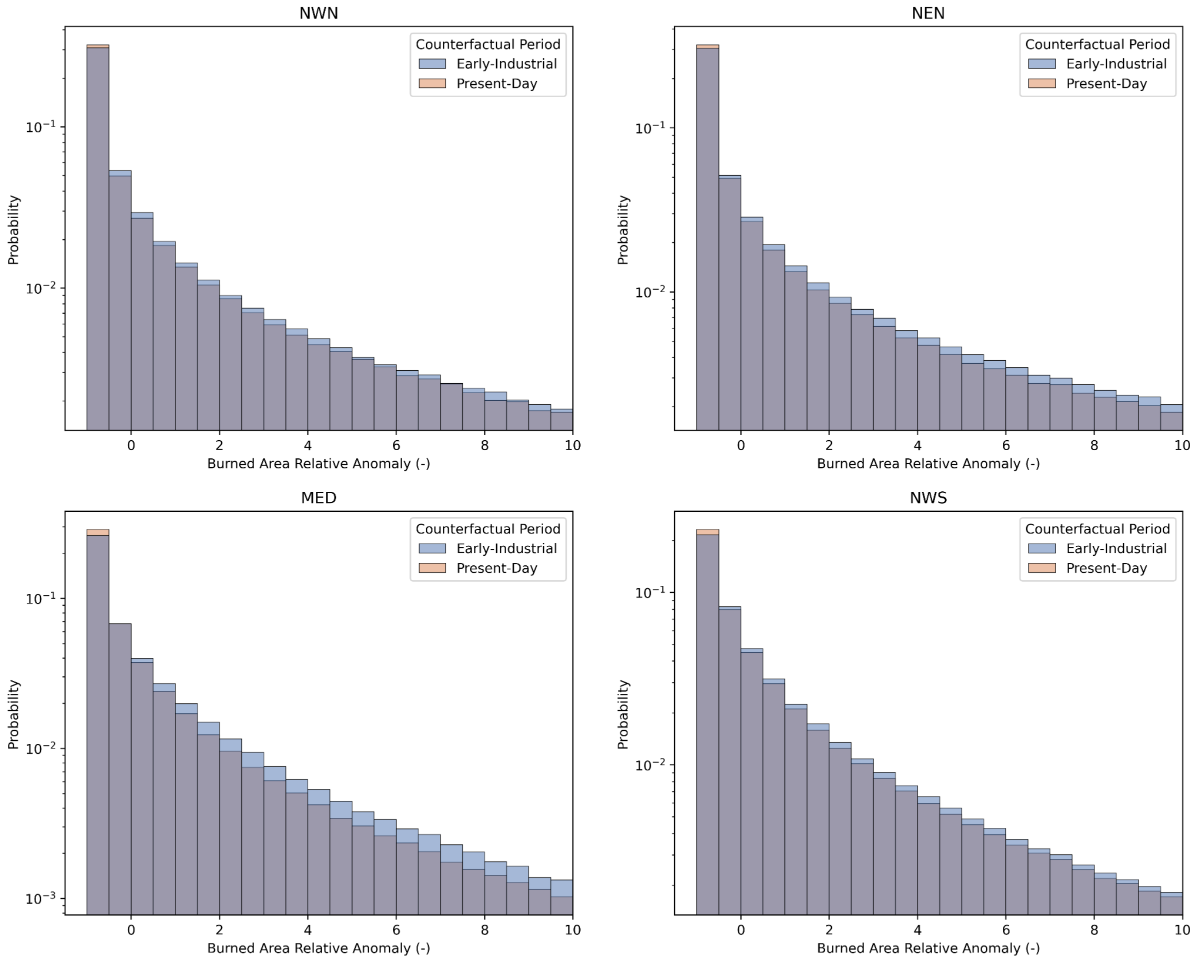

Figure S15: Change in median BA anomaly due to socioeconomic factors (population and land-use change) from FireMIP. Present day BA (2003-2019) for counterfactual (detrended climate, orange) compared to early-industrial (1901-1917) in the counterfactual (detrended climate, blue), for AR6 regions. Top row: North West North America (NWN, LEFT) and North East North America NEN (RIGHT). Bottom row: Mediterranean (MED, LEFT), and North West South America (NWS, RIGHT). Probability is shown on a log scale.

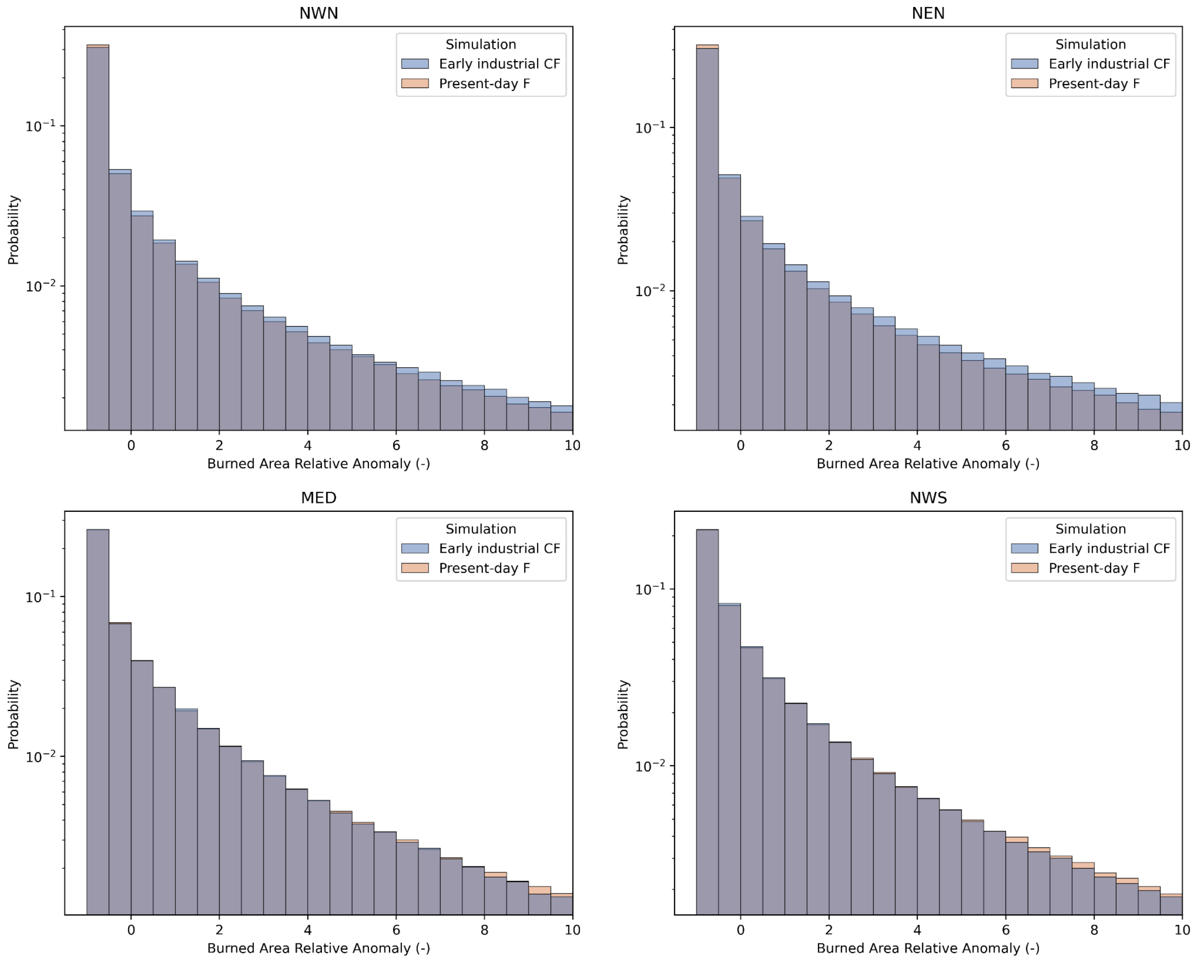

Figure S16: Change in median BA anomaly due to all forcing (climate change and socioeconomic factors) from FireMIP. Present day BA (2003-2019) for factual (historical forcing, orange) compared to early-industrial (1901-1917) in the counterfactual (detrended climate, blue), for AR6 regions. Top row: North West North America (NWN, LEFT) and North East North America NEN (RIGHT). Bottom row: Mediterranean (MED, LEFT), and North West South America (NWS, RIGHT). Probability is shown on a log scale.

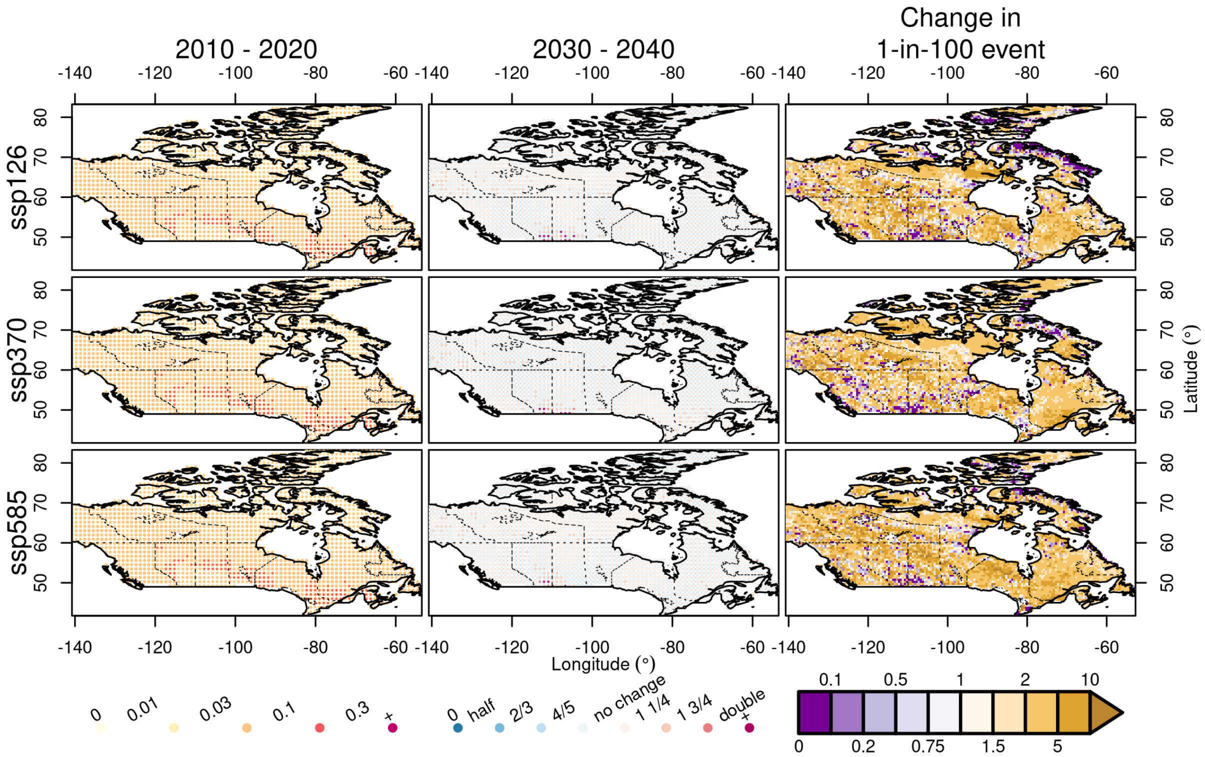

Figure S17: Same as **Figure 18** but covering 2030-2040

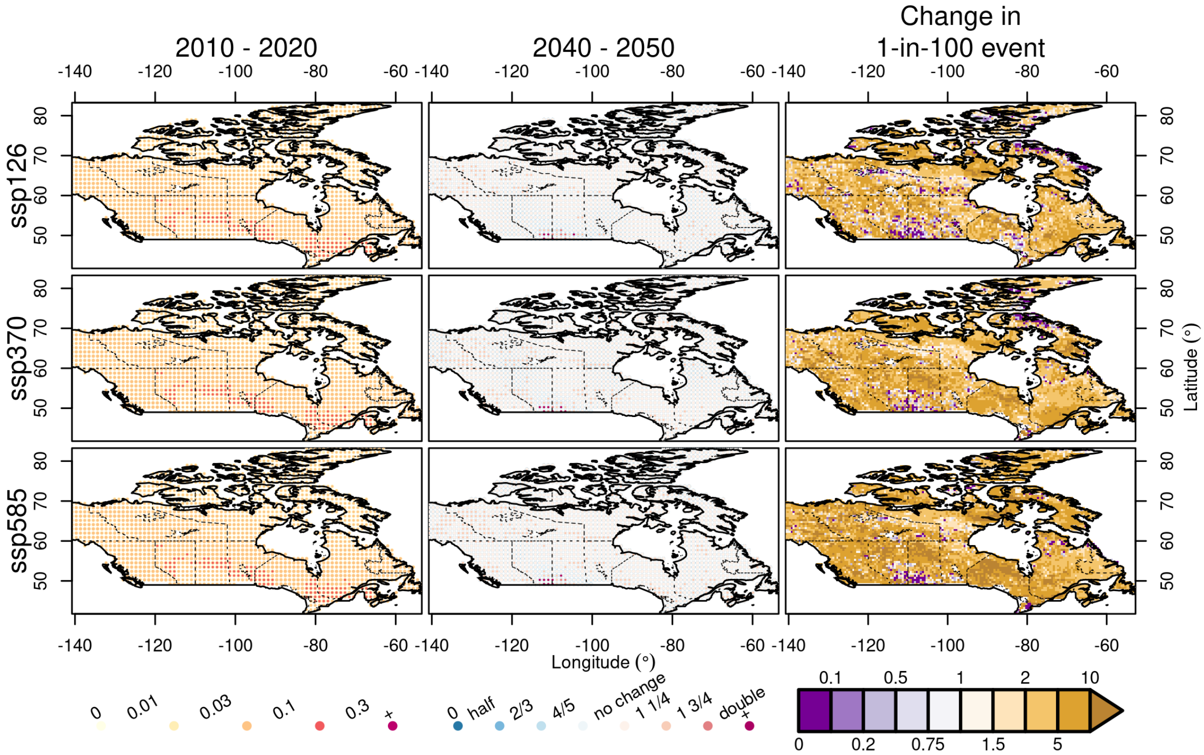

Figure S18: Same as **Figure 18** but covering 2040-2050

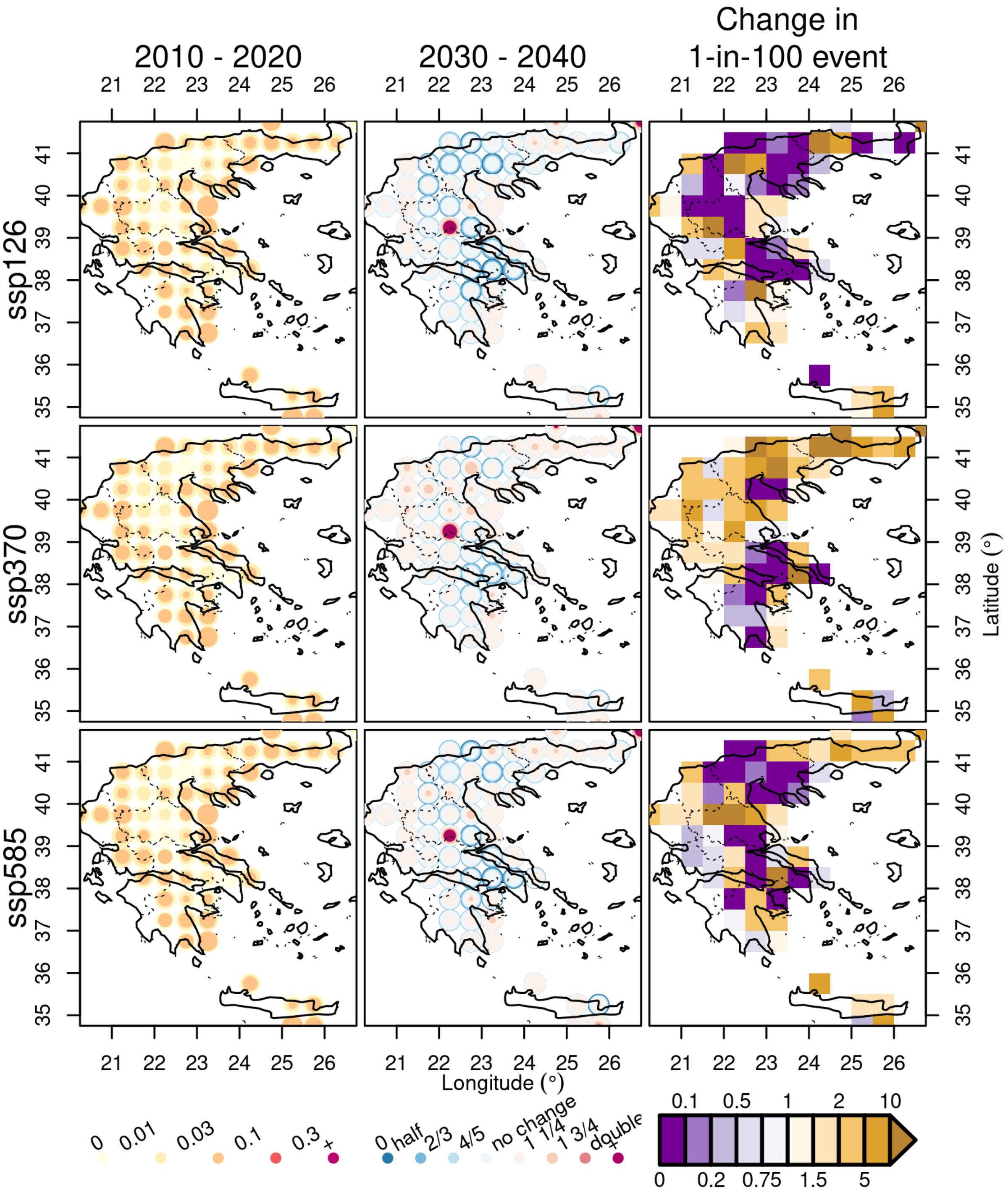

142 **Figure S19:** Same as **Figure 19** but covering 2030-2040

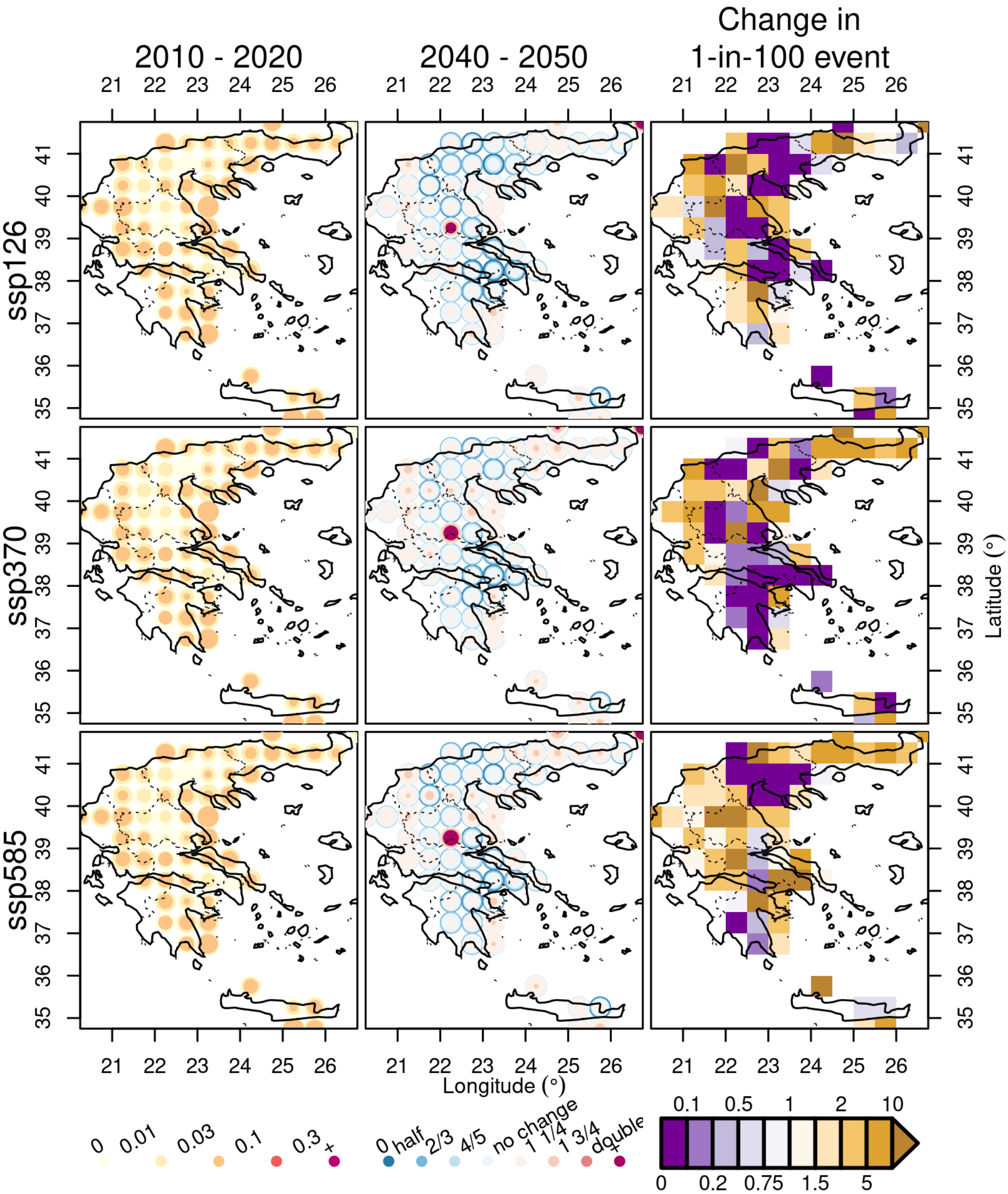

Figure S20: Same as **Figure 19** but covering 2040-2050

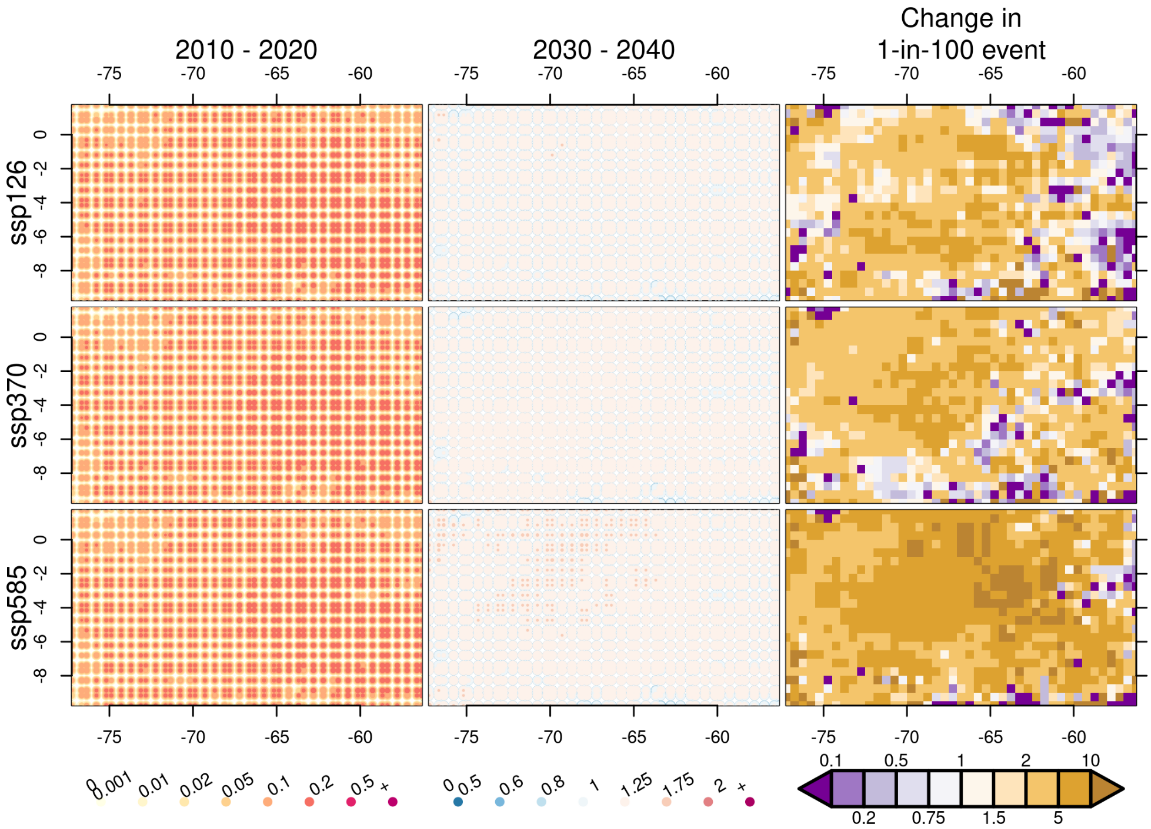

Figure S21: Same as **Figure 18** but Western Amazonia covering 2030-2040 August-October.

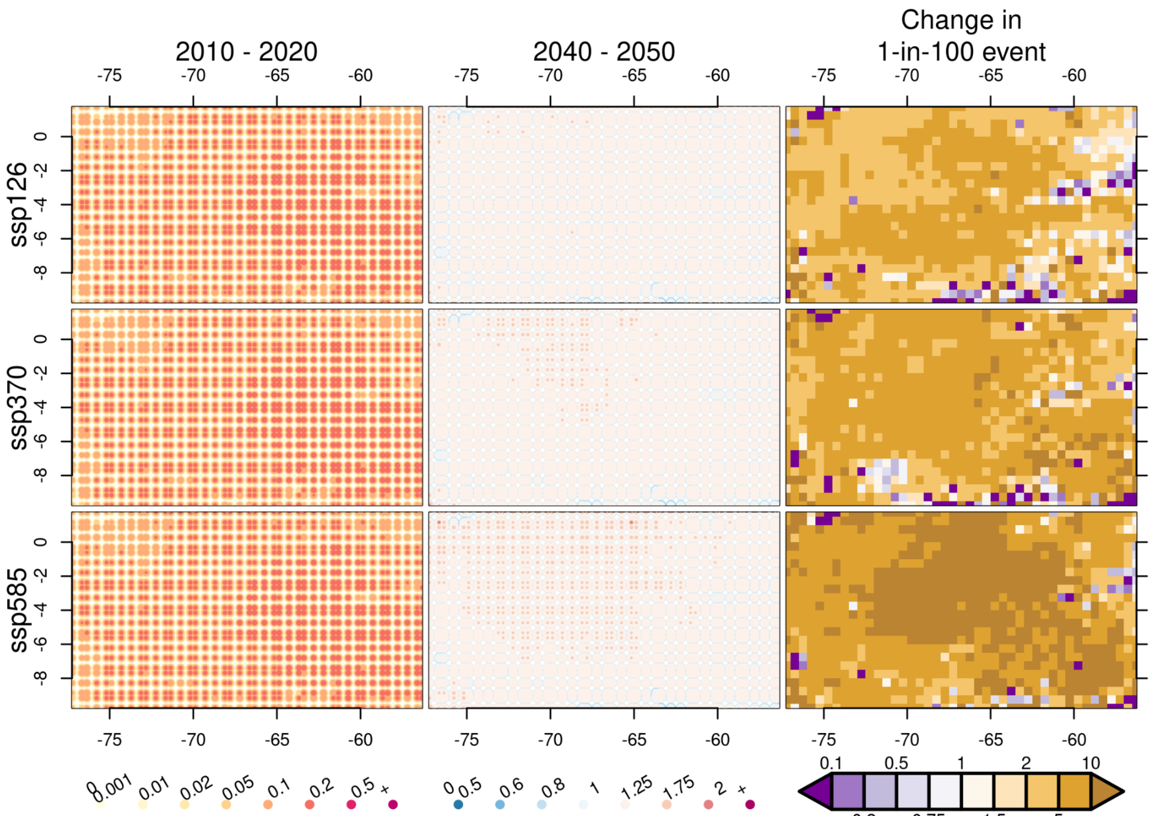

Figure S22: Same as **Figure S21** but covering 2040-2050

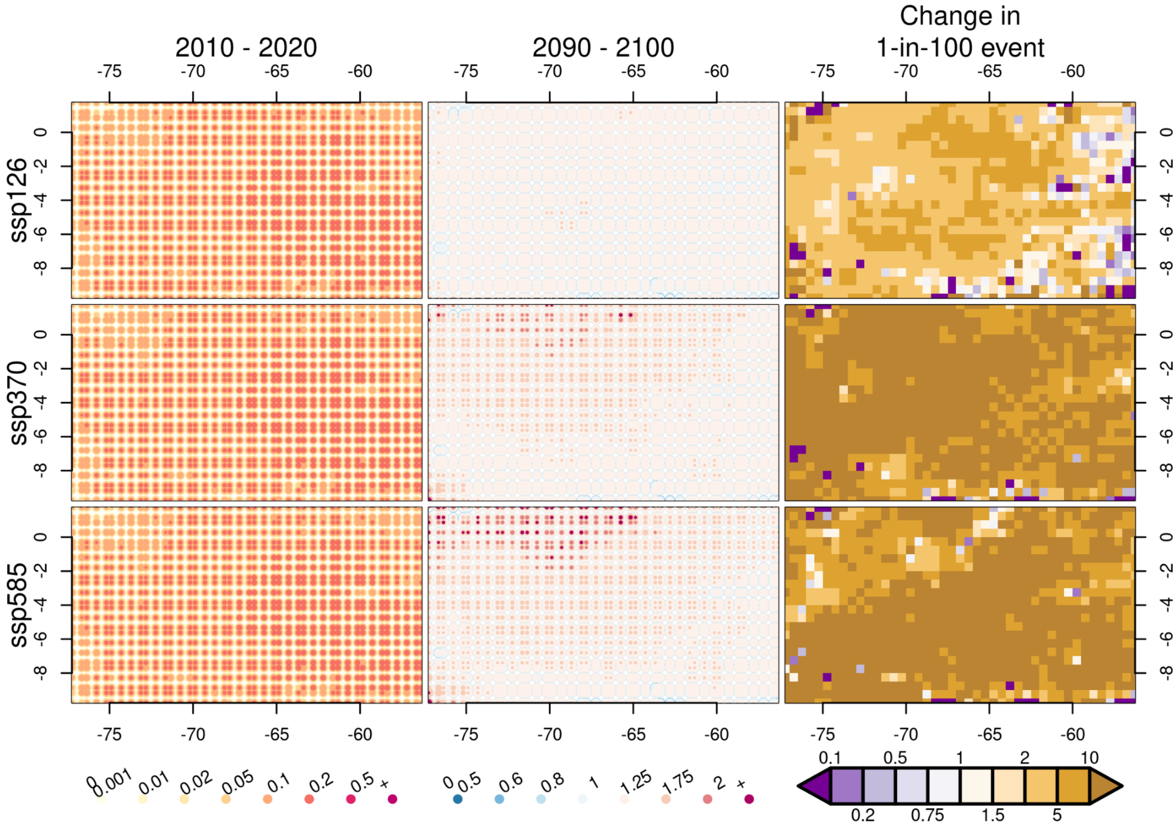

Figure S23: Same as **Figure S21** but for 2090-2100.

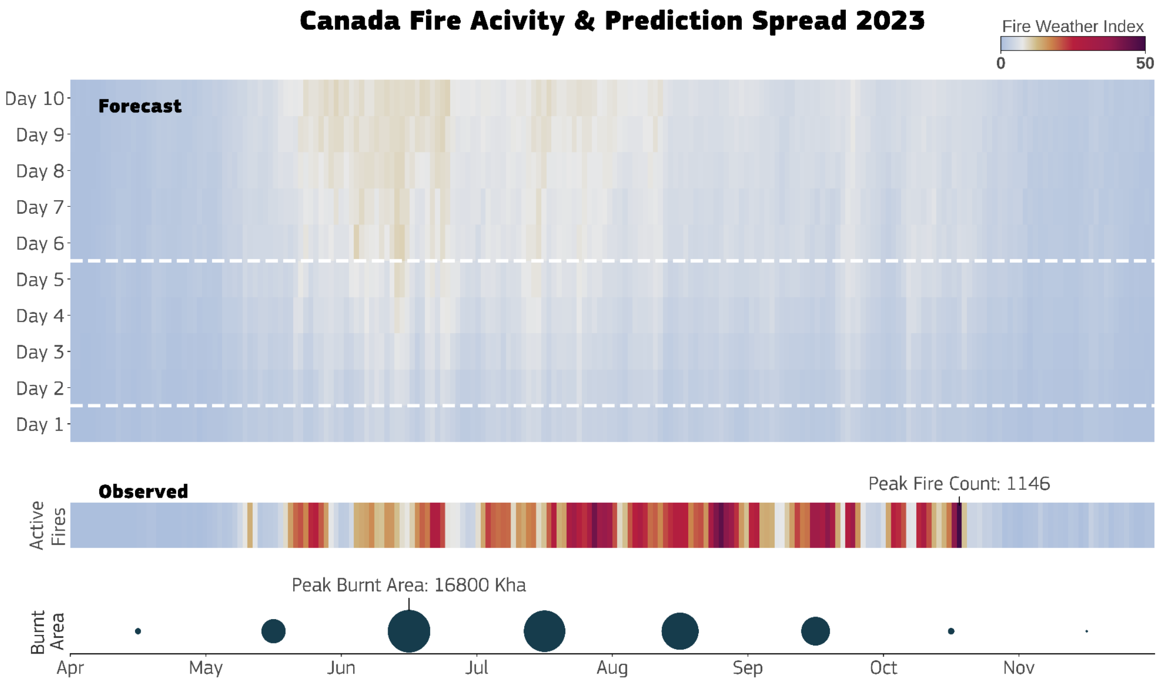

Figure S24: Ensemble spread in the prediction of the FWI in the first 10 days of forecast for Canada. The horizontal lines indicate changes in temporal resolution in the ECMWF weather forecasting systems. The spread accounts for as much as 10%-15% of the predicted values and, as expected, increases with lead time.

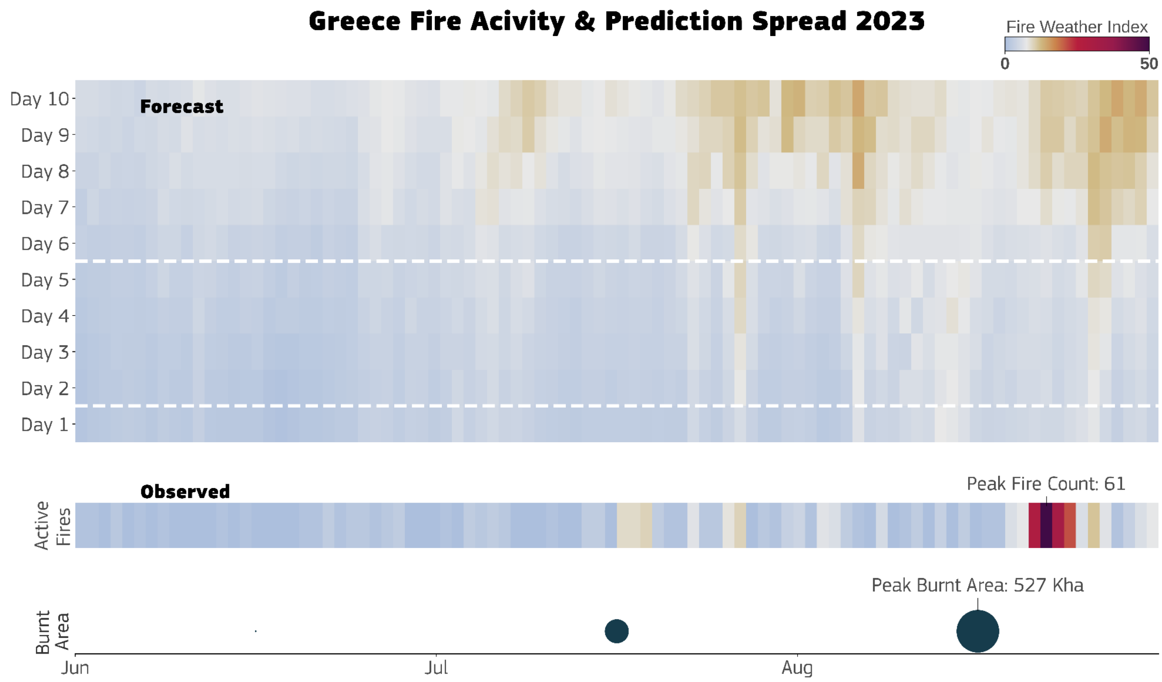

Figure S25: Same as **Figure S24** but for Greece.

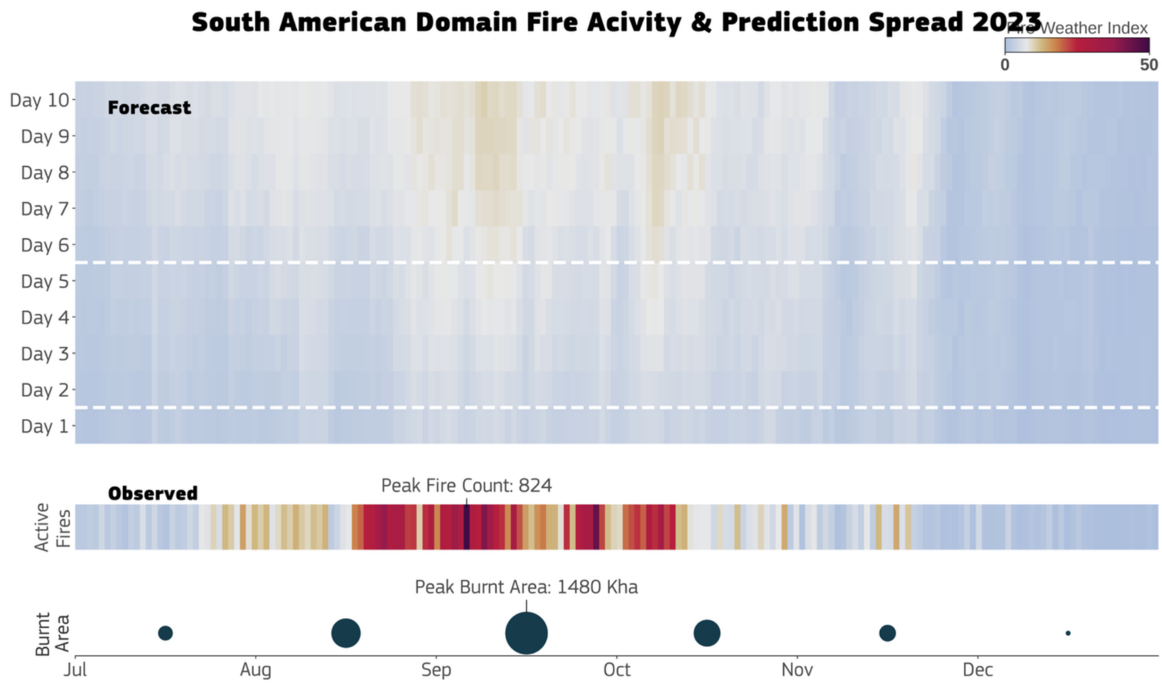

Figure S26: Same as **Figure S24** but for Western Amazonia.

Table S1: Overall PoF driver statistics summary from **Figure 9**. Values refer to variance in active fire counts explained by each control.

	Canada	Greece	Western Amazonia	Target
Weather	43% (Early May) 25% (June-July)	20%(August)	42% (August) 22% (Sept-Oct)	Active fires
Fuel dryness	13% (Early May) 11% (June-July)	9%(August)	26% (August) 10% (Sept-Oct)	
Fuel Abundance	14% (Early May) 12% (June-July)	11%(August)	22% (August) 22% (Sept-Oct)	
Others	29% (Early May) 52% (June-July)	60%(August)	10%(August) 46%(Sept-Oct)	

Table S2: Overall ConFire driver statistics summary from **Figure 10**. Values refer to the median and 5^{th}-90^{th} percentile range of anomalies in burned area caused by each control.

	Canada	Greece	Western Amazonia	Target
Weather	19[5-45]% (May) 16[1-100]% (June-July)	24[4-140] % (August)	14[1-140]% (August) 29[2-45]% (Sept-Oct)	Burned Area Anomaly
Fuel dryness	6[-41-65]% (May) 9[-110-88]% (June-July)	-11[-170-21]% (August)	340[79-400]% (August) 100[62-370]% (Sept-Oct)	
Fuel Abundance	-1[-7- 0]% (May) 1[-3.9- 3.3]% (June-July)	7.5[1-72]% (August)	3[-0-16]% (August) 0 [-1-3.6]% (Sept-Oct)	
Humans	5[1-97]% (May) -0[-25-4]% (June-July)	19[-33 - 220]% (August)	8[1-68]% (August) 3[-1-20]% (Sept-Oct)	

S1. Extended Methods

S1.1 Data and Data Processing

S1.1.1 ConFire vegetation fraction driving data

In **Section 2.4.4.1**, we drive ConFire with tree and non-tree vegetated cover from the Joint UK Land Environment Simulator Earth System impacts model (JULES-ES) at version 5.5 (Clark et al., 2011; Mathison et al., 2023) driven with GSWP3-W5E5 forcings provided at a 0.5° spatial resolution by ISIMIP3a. These runs are freely available at https://www.isimip.org/impactmodels/details/292/. JULES-ES dynamically models vegetation cover in response to meteorology, hydrology, nitrogen availability, and land use change. JULES-ES has been extensively evaluated against snapshots and site-based measurements of vegetation cover and carbon (Mathison et al., 2023; Burton et al., 2022; Clark et al., 2011; Burton et al., 2019; Sellar et al., 2019). JULES-ES-ISIMIP has previously been used as driving data for ConFire to perform future projections (UNEP et al., 2022), though using a previous round of ISIMIP climate forcing (ISIMIP2b). As per (UNEP et al., 2022), vegetation responses to JULES-ES's internal fire model were turned off so as not to double-count the effects of burning. However, in (UNEP et al., 2022), residual JULES-ES simulated biases in vegetation cover were allowed to persist, increasing the uncertainty range of local vegetation cover and resultant burned area responses. We therefore correct the bias in JULES-ES's vegetation cover using a trend-preserving empirical quantile mapping bias adjustment method, implemented using the ibicus software package (Spuler et al., 2024). The bias adjustment method calibrates a mapping between the empirical cumulative distribution function of each surface cover type at each grid cell derived from the JULES-ES model output and the corresponding quantiles in the MODIS remote sensed data at this grid cell over the reference period (2003-2019). The method corrects the bias induced by the JULES-ES model rather than the bias of the climate model, assuming that this has been removed by the ISIMIP3BASD method (Lange, 2019).

The bias adjustment approach maps the empirical cumulative distribution function of each surface cover type at each grid cell derived from the JULES-ES model output to the corresponding quantiles in the MODIS VCF collection 6.1 remote sensed data (DiMiceli et al., 2017) at this grid cell over the reference period (2002-2019). For Canada, where collection 6.1 does not extend north of 60DEG, we used collection 6 (Dimiceli and Others, 2015). This mapping is subsequently applied to the surface information output from JULES-ES driven by climate models over the historical (1994-2014) and future (2015-2099) period. To preserve the trend in the vegetation cover over the future periods, additive detrending of the mean is applied:

$$x_{cm\_fut} \rightarrow F_{obs}^{-1}\left(F_{cm\_ref}(x_{cm\_fut} + \bar{x}_{cm\_ref} + \bar{x}_{cm\_fut})\right) + \bar{x}_{cm\_fut} - \bar{x}_{cm\_ref} \qquad (1)$$

Here F_{cm_ref} is the empirical cumulative distribution of the model over the reference period, ${F^{-1}}_{obs}$the inverse cumulative distribution function of the observations, x_{cm_fur} the quantile that is adjusted and $\underline{x}_{cm\_ref}$ and $\underline{x}_{cm\_fur}$ the means of the model output over the reference and future periods. This mapping is applied over a rolling window of 9 years over the future period.

The approach ensures that not only the mean but also the shape of the distribution is corrected without assuming a parametric form, whilst also preserving additive trends driven by the future climate model. Furthermore ensures continuity between the historical and future period by using a rolling window over the future period.

The results were evaluated in terms of the ability of the bias correction method to reduce the model bias over the historical period, as well as preserve the trend between the future and historical period. It was found that the method corrects the bias well over the historical period for most regions, variables and gridcells in both the mean and 80th percentile at each grid cell. The trend between the future and historical period is well preserved in most regions and gridcells, with less than 0.1% of gridcells overall experiencing an absolute trend modification larger than 5%.

To demonstrate the evaluation conducted, **Figure S24** shows the results for treecover over North-Western Canada. The plots for the remaining regions, including tree and no-tree cover, can be found in a notebook https://github.com/jakobwes/State-of-Wildfires---Bias-Adjustment. Investigating the timeseries of average treecover over the region, we find that the correction method reduces the bias over the historical period and matches the future period to the historical period (**Figure S24**a). The cumulative distribution functions of average tree cover merged over all spatial locations in observations and model match better after bias adjustment (**Figure S24b**). They do not match perfectly, and we note that this is a non-calibrated aspect that we do not expect to have zero bias but that is important to evaluate. Furthermore, we find that the improvement in both mean and 80th percentile hold across the region (**Figure 19c**). The trend between future and historical period is preserved for the majority of grid-cells, with the absolute change in trend being close to zero for most grid-cells.

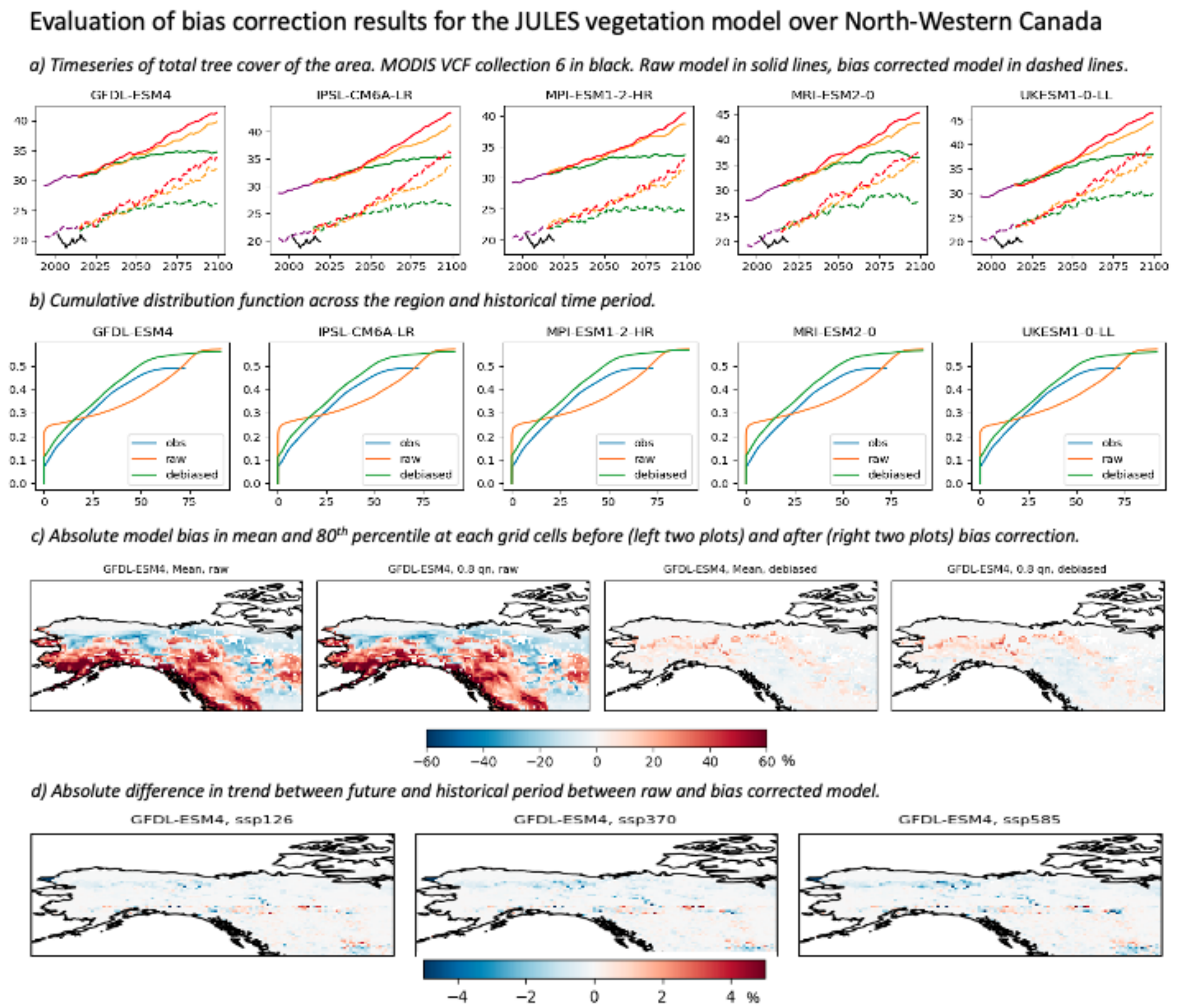

Figure S24: Evaluation of the JULES vegetation model bias adjustment for tree cover over North-Western Canada. a) Timeseries of tree cover over the area for different climate models both with historical and scenario runs, raw model in solid lines, bias corrected models in dashed lines and MODIS VCF in black. b) Cumulative distribution function of tree cover values across region and historical time period for different climate models for observations (blue), raw models (orange), debiased models (green). c) Absolute model bias in mean and 80th percentile for the GFDL-ESM4 climate model before (left two plots) and after bias adjustment (right two plots). d) Absolute difference in trend (difference between future and historical period) between raw and bias corrected GFDL-ESM4 model for ssp126, ssp370 and ssp585 scenarios.

S1.2 Modelling Frameworks

S1.2.1 PoF

The Probability of Fire (PoF) system uses gradient-boosted decision trees to provide a probability forecast of active fire occurrence (McNorton and Di Giuseppe, 2024). The supervised algorithm which trains an ensemble of decision trees uses regularization techniques to prevent overfitting (Chen & Guestrin, 2016). The training, based on 2010-2014 MODIS active fire detections, classifies a positive fire event as any detection within a 9 km grid cell.

The relative contribution of each input control to the model prediction is evaluated using Shapley values, computed using the Shapley Additive exPlanations python library (Lundberg & Lee, 2017). The SHAP value indicates the importance of each feature in a model, where a positive SHAP value reflects a positive impact on the model prediction and a negative SHAP value reflects a negative impact. Specifically for this study we use the TreeExplainer, which computes the SHAP values by interrogating the structure of the decision trees within the model based on the input feature values. The probability controls are then normalised and grouped into the four categories given in **Table 3** of the main text. By combining these with the total amount of fires predicted for a given area we can attribute those fires into one of the four controls. The 'Other' control also includes fire occurrences not predicted by the model. This is computed given by:

$$Other = SHAP[Other] + max\,(0, Area\_Total\_Fires\_Observed - Area\_Total\_Fires\_Predicted) \tag{2}$$

Where, SHAP[Other], is the contribution of the 'Other' control to the total predicted fires for a given region and, $Area\_Total\_Fires\_Observed$ and $Area\_Total\_Fires\_Predicted$ are the total number of observed and predicted fires for the same region.

S1.2.2 ConFire

ConFire is a burned area attribution tool, used for trend detection and attribution (Kelley et al., 2019), event attribution (Kelley et al., 2021) and future projections (UNEP et al., 2022). ConFire finds the likelihood of causes of or changes in BA by optimising a simple, semi-empirical process representation model by applying Bayes Theorem. In our case, Bayes Theorem states that the likelihood of a model configuration described by a parameter set $\{\beta\}$ and monthly explanatory variables (i.e model driving data) $\{X_{iv}\}$ given some training observation of monthly burned area fraction $\{Obs_i\}$ from MODIS MCD64A1, for cells *i*, is proportional to the prior probability of $\{\beta\}$ ($P(\{\beta\})$) multiplied by the probability of the observations given that model configuration:

$$P(\{\beta\}|\{Obs_i\},\{X_{iv}\}) \propto P(\{\beta\}) \times P(\{Obs_i\} \mid \{X_v\},\{\beta\}) \tag{3}$$

We use the zero-inflated logit distribution introduced by (Kelley et al., 2021) as our update distribution, as this is specifically designed to better represent the tails of the distribution during fire events:

$$P(\{Obs_i\} \mid \{X_{iv}\},\{\beta\}) = \prod_i^N P(Obs_i| \{X_v\}_i,\{\beta\})$$

$$P(Obs_i = 0 \mid \{X_v\}_i,\{\beta\}) = (1 - M(\{X_v\}_i,\{\beta_M\})^{p_1}) \times (1 - P_0)$$

$$P(Obs_i > 0 \mid \{X_v\}_i,\{\beta\}) = (1 - P(Obs_i = 0 \mid \{\beta\})) \times \aleph(logit(Obs_i) - logit(M(\{X_v\}_i,\{\beta_M\})),\sigma) \tag{4}$$

where $\{\beta_M\}$ is the set of parameters related solely to the underlying model, M, $logit(x) = log\left(\frac{x}{1-x}\right)$, P_0, P_1 and σ are parameters within the full set $\{\beta\}$ which describe the model error and $\aleph(\mu, sd)$ is a normal distribution with mean of $\boldsymbol{\mu}$ and standard deviation of sd.

The model, *M*, simulates fractional BA (fraction) via a number of controls. For attribution and outlook, these controls follow (Kelley et al., 2021; Burton et al., 2019): Fuel load, fuel moisture, ignitions and suppressions. This follows the general model structure of global fire models (Hantson et al., 2016; Rabin et al., 2017) and is most appropriate for looking at long term, coarse fire drivers (Moritz et al., 2005). For driver assessment, we separate out an additional control for “fire weather” and introduce a “snow cover” control. Model BA is the product of these controls, *c*:

$$M(\{X_v\},\{\beta_M\}) = F_{max} \times \prod_{c} f(\{X_c\},\{\beta_c\}) \quad (5)$$

Where F_{max} describes maximum monthly burned area fraction and is an optimizable parameter in set $\{\beta_M\}$, $\{X_c\}$ are the BA driving variables, $\{\beta_c\}$ the parameters related to control c and *f* is the function that describes the control influence on BA. Each control describes the expected BA if all other controls imposed no limitation on burning - for example, when *c* is fuel, $f(\{X_c\},\{\beta_c\})$ describes the BA in perfectly dry conditions with saturated ignitions and no suppression. To achieve this, *f* is the logical function:

$$f(\{X_c\},\{\beta_c\}) = 1/\left(1 - exp\left(-\beta_{c,0} - \sum_{j} \beta_{c,j} \times X_j\right)\right) \quad (6)$$

where $\beta_{c,j}$ is the contribution of driving variable X_j to the control and $-\beta_{c,0}$ is a parameter that can shift the midpoint of the sigmoid curve.

All variables X_v where normalised to be between $[0, 1]$ based on the training data to aid priors selection and optimization - though analytically this should have no impact on our results. Our priors fix the direction each drive can influence a control (drivers and direction are listed in Table 3 and 5) but beyond this relatively uninformed. Priors for $\beta_{c,j}$ where described by a log-normal distribution with a μ of 0 and σ of 10, and set to be positive for liberative drivers (one that increases the strength of a control) and negative for suppressive (ones that reduce the strength of a control). $\beta_{c,0}$ priors were set to a normal distribution with a mean of 0.5 and a standard deviation of 1. F_{max} and P_0 priors were set as a uniform distribution between 0 and 1 $\boldsymbol{\sigma}$ was set to a half-normal with mean of 0 and standard deviation of 10.

We sampled the posterior distribution using Bayesian inference following a similar protocol to (Barbosa, 2024) with the pymc python package version 5 (Abril-Pla et al., 2023), employing 100 chains each over 1000 warm-up iterations (that were not subsequently used) and 100 sample iterations using the No-U-Turns Hamilton Monte Carlo sampler (Hoffman and Gelman, 2011) while utilising 50 % of the data or a minimum of 6000 grid cells. To sample the posterior distribution, we then randomly sample 50 iterations from each chain, thereby approximating the posterior with 1000 ensemble members. As per Barbosa (2024), for evaluation (**Figure S28-S39**) we trained the first half of the period and tested on the second half. For the rest of the results, we trained on the full period.

We obtaining probability distributions from the model posterior for our results, ConFire offers two probability, which we have adapted slightly from (2021) :

1. The likelihood of different levels of burning for a specific event (i.e a grid cell in a given timestep) which considers uncertainty explained by the model and residual uncertainty described by our error parameter, $\boldsymbol{\sigma}$. We use this when we are comparing a single grid of cells and months, such as for evaluation, and for assessing the un. The likelihood of a Burned Area, *BA*, under drivers, *X*, which can be out-of-training sample, is:

$$P(\,BA|\,(X_v,\ \beta|\ \{Obs_i\},\{X_{iv}\}))\ =\ \int_{\beta} P(\beta|\ \{Obs_i\},\{X_{iv}\})\ \times P(BA|\beta)\,d\beta \quad (7)$$

Where $P(BA|\beta)$ is take from equation 4.

When building distributions for multiple grid cells or time periods, as with building a climatology in **Section 3**, we convolute the probability distributions of individual time periods and cells following equations in (Kelley et al., 2021). Converting probabilities over a large number of cells gives us the second measure.

The emergent probability of different mean levels of BA over many events explained directly by the model and its driving variables. We use this when assessing the emergent likelihood of burning in **Section 4** and **Section 5**. This is the same as taking the mean of *n* simulations in equation 7 as *n* tends to infinity. Doing this, $P(\{Obs_i\} \mid \{X_{iv}\}, \{\beta\})$ from equation 4 will tend towards a BA of model *M* output weighted by the likelihood of a zero BA:

$$D(BA) = \lim_{n\to\infty} \left[\sum_{i=1}^{n} P(\, BA \mid (X_v, \quad \beta \mid \{Obs_i\}, \{X_{iv}\})) \,/\, n \right]$$

2.

$$= \int_{\beta} M(\{X_v\}_i, \{\beta_M\}) \times (1 - M(\{X_v\}_i, \{\beta_M\})^2) \times (1 - P_0)\, d\,\beta \qquad (8)$$

For attribution and future projections, ConFire produces correctly ranked by consistently biassed probability distributions (**Supplement Section "Change in Likelihood of High Burned Area in 2023 due to Total Climate Forcing and Socioeconomic factors"**). The final step is therefore to introduce a correction factor. As this distribution bias is constant across the observed BA distribution, a simple scaling factor is all that's needed. To do this, we assign the likelihood associated with the BA in equation 8 with a scaled burned area (BA^*) so that the mean of the sample distribution matches the mean of the observation for the period 2003-2019.

$$BA^* = BA \times \Sigma(\{Obs_i\} \,/\, \int_0^1 D(BA) \times BA\, dBA \qquad (9)$$

BA^* is then used in equation 8.

S1.2.3 Attributing Fire Weather

Bias Correction

We evaluated the individual variables in the FWI (see evaluation), and found that each variable was slightly biased compared to ERA5 reanalysis. We therefore applied a bias correction to the final FWI, rather than bias-correcting each individual variable.

We bias-corrected the HadGEM3 2023 large ensemble based on a bias assessment of the 15 historical members from 1960-2013 vs. ERA5 observation-driven FWI, using a simple linear regression on *fwi* transformed using:

$$fwi_* = log(exp(fwi) - 1) \qquad (10)$$

to remove the physical bound at 0. We use this instead of using a straight *log* transformation as it ensures numerical stability at higher values, crucial when dealing with extreme FWI values, thereby avoiding blow-up effects. It also preserves the extreme tail of the FWI distribution, allowing us to accurately capture and analyse critical events associated with high fire risk..

We perform a simple linear regression on ERA5 and on each historical member to obtain the basic regression parameters:

$$fwi_* \sim fwi_{*,0} + \Delta_{fwi} \times t \qquad (11)$$

Where t is time, and t = 0 is set to 2023, Δ_{fwi} is the rate of change, or trend, of fwi_* and $fwi_{*,0}$ is the estimated $fwi_*$for 2023. Our bias correction is therefore based on present-day levels of warming, taking account of the additional warming from 2013-2023 (assuming the trend from 1960-2013 continues to 2023 linearly). If anything this is likely conservative given that warming rates may have increased more rapidly in the last 10 years.

We generate the bias-corrected 2023 ensemble by correcting each of the 525 present-day ensemble members against each of the 15 historical members (creating an ensemble of 7875 members). Due to the perturbation procedure used to generate the 2023 ensemble from the historic (Ciavarella et al., 2018), we can not assume that present-day members pair to historical members. We therefore iterate over all possible pairs:

$$fwi_{corrected} = (fwi_{*i} - fwi_{*0,j}) \times \sigma(fwi_{*era5}) / \sigma(fwi_{*j}) + fwi_{0,*\,era5} \qquad (12)$$

$$\sigma_{\Delta}(fwi_*) = sdev(fwi_* - \Delta_{fwi} \times t)$$

Where i is a present-day ensemble member, and j is a historical member.

We finish by applying the inverse of the transformation from equation 10 :

$$fwi_{corrected} = log(exp(fwi_{*,corrected}) + 1) \qquad (13)$$

Probability Ratio

We use the ERA5 2023 FWI for our event threshold in each region, using the month of peak anomaly from **Figure S2** in each region. We use this threshold to calculate the probability ratio (PR) of the event occurring with and without climate change. To calculate the PR, we find the number of ensemble members that exceed the 2023 ERA5 FWI value in the bias-corrected ALL simulation, and divide this by the number of members that exceed the same value in the bias-corrected NAT simulation, bootstrapping 10,000 times to giving the probability of exceeding the observed 2023 FWI value in a world with and without climate change plus uncertainty bound for the 5-95th percentile.
PR = p(ALL) / p(NAT)

S1.2.4 FireMIP

For the multi-model ensemble we use simulations from the ISIMIP3a fire sector, as published in (Burton & Lampe et al. 2023). The 7 models reporting BA for ISIMIP3a are shown in the table below. The methodology follows the ISIMIP3a Impacts Attribution protocol, as outlined in (Mengel et al., 2021), where the factual historical simulations are driven with GSWP3-W5E5 reanalysis data, and the counterfactual simulations are the same historical data which has been detrended via quantile mapping (Mengel et al., 2021).

As outlined in (Hantson et al., 2016), the spread in the absolute BA is large amongst the observations, models and regions and therefore a normalised relative anomaly (RA) rather than absolute BA is used for the analysis. To calculate the RA in present day BA, we subtract the counterfactual mean, and divide by the counterfactual mean. By comparing both factual and counterfactual experiments to the counterfactual mean, we are looking at the fractional increase in BA driven by climate change compared to a baseline without climate change. Based on model performance by AR6 region, a region-specific weighting is also applied following (Knutti et al., 2017). The weighting is based on the model's distance to the observed BA temporal RA using both FireCCI5.1 and GFED5, measured using NME as per (Kelley et al., 2013). To measure the uncertainty, random noise is generated and scaled by the climatological RMSE of each model. This noise is then added to the modelled relative anomaly, this process is repeated 1000 times. This performs the same function and the uncertainty quantification from model error as Equation 4 does for ConFire Then, bootstrapping is applied to the monthly regional BA RA (now with noise added in) according to the weight for each model. Uncertainty is calculated by taking the 2.5-97.5th percentile of the resultant histogram. All results are reported as P50 [P2.5, P97.5]. The methods are explained in full in (Burton & Lampe et al. 2023).

Table S3: FireMIP Models used for attributing median burned area. Table reproduced from (Burton & Lampe et al. 2023)

Model		CLASSIC	INFERNO	LPJ-GUESS-SIMFIRE-BLAZE	LPJ-GUESS-SPITFIRE	ORCHIDEE-MICT-SPITFIRE	SSiB4/TRIFFID	VISIT
Fire Model		CLASSIC	INFERNO	SIMFIRE	SPITFIRE	SPITFIRE	Li	After (Thonicke et al., 2001)
Land / Vegetation		CLASSIC	JULES	LPJ-GUESS	LPJ-GUESS	ORCHIDEE	SSiB	VISIT
Dynamic Veg	**Physiology**	Yes	Yes, via TRIFFID	Yes	Yes	Yes	Yes, via TRIFFID	Yes
	LAI	Yes	Yes, via TRIFFID	Yes	Yes	Yes	Yes	Yes
	Bio-geography	No	Yes, via TRIFFID	Yes	Yes	Yes	Yes	No
Nitrogen Cycle		Yes	Yes	Yes	Yes	No	Yes	Yes, but C-N coupling is limited
No. PFTs		9	13	17	17	19	7	33 (biome types)
No. Soil Layers		20	4	2	2	11	3	2
Fuel		Vegetation and litter	Vegetation & top soil layer as proxy for litter	Vegetation, litter	Litter	Vegetation and litter	Vegetation and litter	Litter
Ignitions	**Natural**	Prescribed lightning	Prescribed lightning	SIMFIRE describes annual BA + fire-climatology -> daily BA used as Fire-Probability	Prescribed lightning	Prescribed lightning	Prescribed lightning	Probabilistic based on fuel wetness

	Anthropogenic	Prescribed population density	Prescribed Population density	SIMFIRE includes suppression by humans	Prescribed population density	Prescribed population density	Prescribed population density	No
Suppression		Prescribed population density	Crops, population density	Crops (100%), prescribed population density (Hyde3.1)	Crops, population density	Prescribed population density, crops	Prescribed population density and GDP	Low fuel load
Spread		Wind speed and soil moisture	None	Daily BA (no explicit spread)	Rothermel equations including wind speed, tree fraction, grass fraction, fuel moisture, fuel load and characteristics	wind speed, tree fraction, grass fraction, fuel moisture, fuel load	Wind speed and soil moisture	None
Model inputs		SW & LW radiation, precipitation, air temperature, specific humidity, wind speed, atmospheric pressure, population density, lightning	SW & LW radiation, precipitation, air temperature, specific humidity, wind speed, population density, lightning	SW radiation, precipitation, air temperature (mean, min, max), relative humidity, wind speed	SW radiation, precipitation, air temperature, specific humidity, wind speed, atmospheric pressure, population density, lightning	SW & LW radiation, precipitation, air temperature, specific humidity, wind speed, atmospheric pressure, PFT map, population density	SW & LW radiation, precipitation, air temperature, specific humidity, wind speed, atmospheric pressure, population density, and GDP, peat map, land cover change	Air temperature, precipitation, air vapor pressure, cloudiness, wind
Resolution		1 deg	0.5 deg	0.5 deg	0.5 deg	0.5 deg	0.5 deg	0.5 deg
References		(Melton et al., 2020)	(Burton et al., 2019, 2020; Mangeon et al., 2016)	(Rabin et al., 2017; Smith et al., 2014; Knorr et al., 2014)	(Rabin et al., 2017; Smith et al., 2014; Thonicke et al., 2010; Lehsten et al., 2009)	(Yue et al., 2014, 2015)	(Huang et al., 2021, 2020; Li et al., 2012; Hugelius et al., 2013; Li et al., 2013)	(Ito, 2019)

S2. Evaluation

S2.1 POF

The PoF model, trained on observed fire activity, provides a daily probability of fire occurrence based on the input variables described in **Table 3** of the main text. The three cases explored in the main study can be visualised as fire risk maps at a 1 km resolution, higher than the 9 km used for attribution. The 1km predictions show that whilst PoF often fails to capture the true total number of active fires, the relative attribution is likely to be accurate given by the models ability to capture the spatiotemporal pattern of fire activity reflected by the forecast danger shown in the figures below. Of the three case studies the model accurately reflects fire activity for Canada and Western Amazonia, and whilst high fire danger is modelled over Alexandroupolis, Greece, it fails to capture the severity of the event.

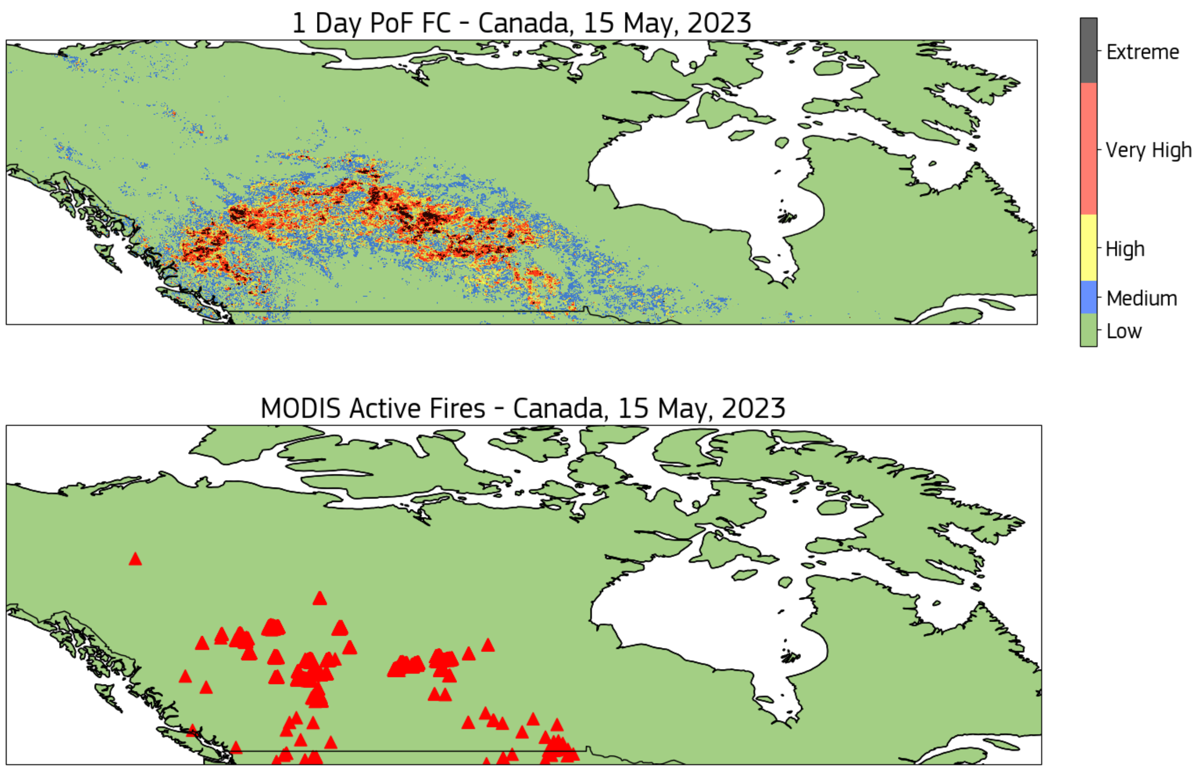

Figure S25: Spatial representation of the day 1 PoF forecast at ~1km resolution expressed as a danger rating for the 15th May over Canada (top). MODIS active fire detections for the same day and domain (bottom).

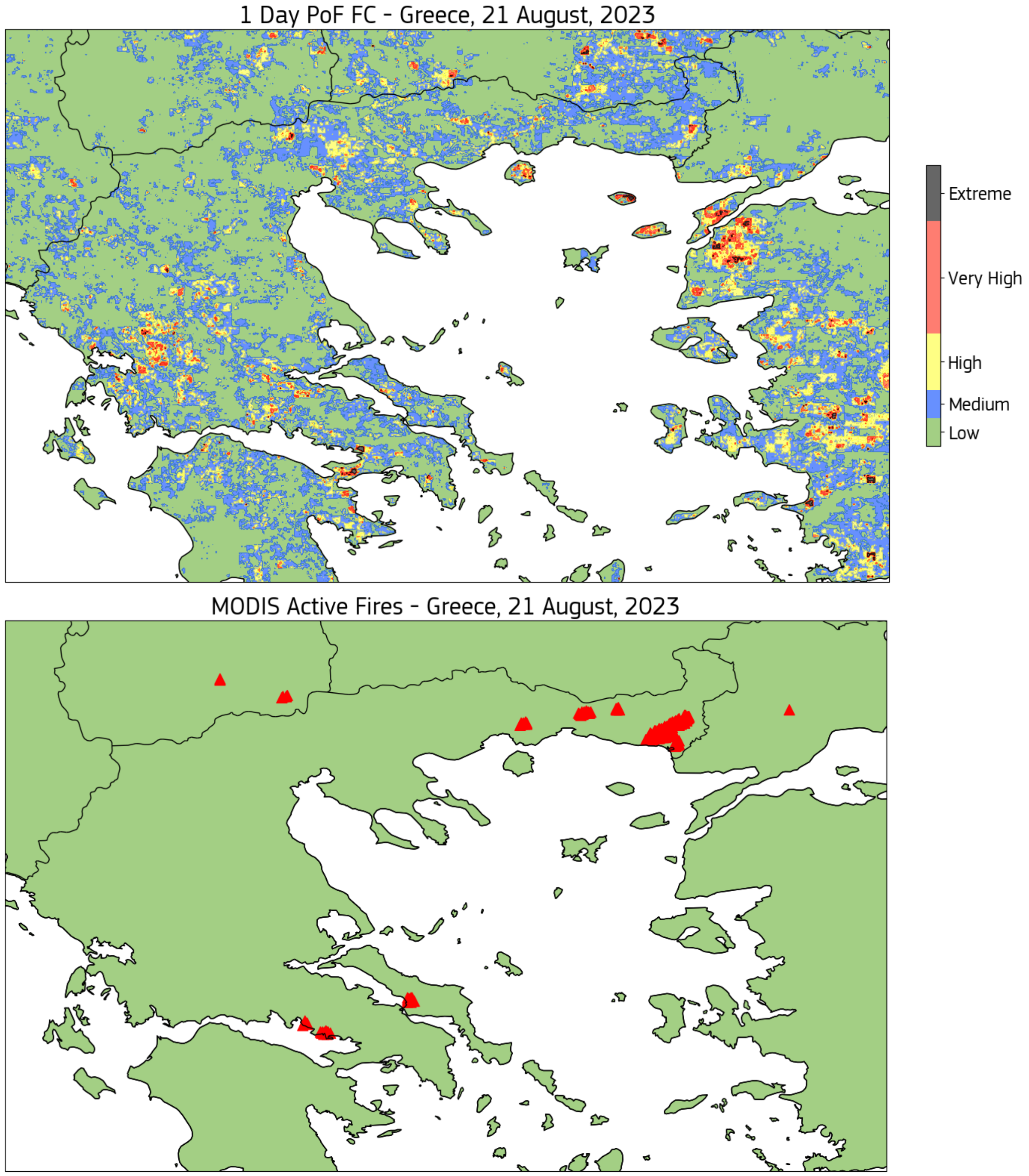

Figure S26: Spatial representation of the day 1 PoF forecast at ~1km resolution expressed as a danger rating for the 21st August over Northern Greece (top). MODIS active fire detections for the same day and domain (bottom).

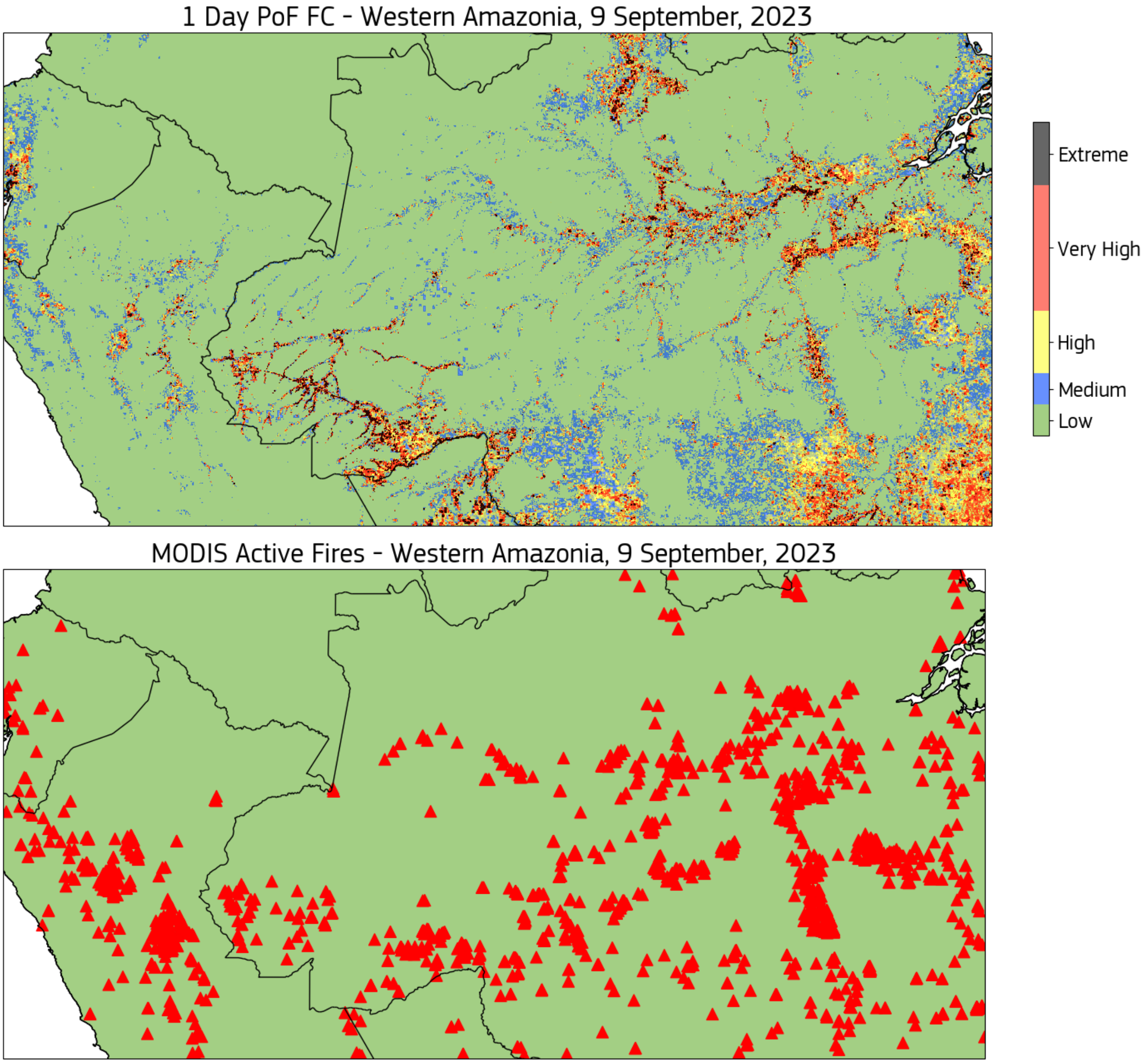

Figure S27: Spatial representation of the day 1 PoF forecast at ~1km resolution expressed as a danger rating for the 9th September over Western Amazonia (top). MODIS active fire detections for the same day and domain (bottom).

S2.2 ConFire

The ConFire model simulates a probability distribution of BA which, unlike most numerical or ensemble-based models, requires a probabilistic technique for evaluation.
The uncertainty range of the ConFire is crucial for the analysis in this study. We obtain confidence in our results by seeing if the shift of the model's probability distributions is significant compared to the size of the uncertainty of that distribution. Suppose the uncertainty range is larger than any change when testing for i.e, attributing with or without climate change, future changes, or seasonal anomaly. In that case, the framework will tell us, and our results will show that these are unlikely/not significant. Conversely, if the change in distribution is larger than the model's uncertainty range, we can make a confident statement even if that model is uncertain.

As the precision of the modeling framework is inherent in the analysis itself, the main aspect to evaluate is the ability of the model's probability distribution to represent the range of uncertainties when tested against observations accurately. To do this, we followed the evaluation procedure outlined in (Barbosa, 2024), which we summarise here.

We trained the model during the first half of each period used in the analysis and performed subsequent evaluations on the second half. The training period for near-real-time driver assessment was 2014-2018, and for the attribution/future projections run, 2003-2011. The evaluation period was 2019-2023 for driver assessment and 2012-2019 for attribution/future projections. Using a different period from the optimization ensures an independent model evaluation and provides an indication of how well the framework captures uncertainty in out-of-temporal sample observations.

The FLAME system (Barbosa, 2024) that we merge with ConFire automatically generates a series of evaluations which we show for region region in turn in the subsequent two sections. While the techniques are outlined in (Barbosa, 2024), these automated figures have not previously been published. So alongside the evaluation procedure below is a guide to interpret if these plots show a good model performance.

For the evaluation period, we assess how well the model predicts new observations by testing how likely the observations are given the optimized model (equation 7). While this sounds counter-intuitive, we do this rather than test the model given the observations because the model doesn't yield a single answer or a set of numbers, but rather a distribution of model parameters and output, reflecting inherent uncertainty in the processes. This approach allows for comprehensive testing of the entire model's posterior probability distribution at once and provides insight into the model's ability to generate the observed distribution and capture the uncertainty in the modeled process. We approximate the probability of an observation given our model by sampling 10 parameter ensemble members from each of our 100 chains, providing us with 1000 ensemble members, and sample the likelihood as per (Kelley et al., 2021). The example below, taken from **Figure S32**, shows how we summarise this for each observation (scatter plot left) and all observations in a time series for each cell (middle and right). If the model performed perfectly, the probability of the observations given the model will all be close to 1, as the scatter plot indicated for BA fractions above ~ 0.0003. The model won't always capture the uncertainty required to generate the observations. This generally happens at specific burned areas (like low ones in this example). Areas where this happens often are highlighted on the map with the map in the middle showing the performance at the 5th percentile of the time series.

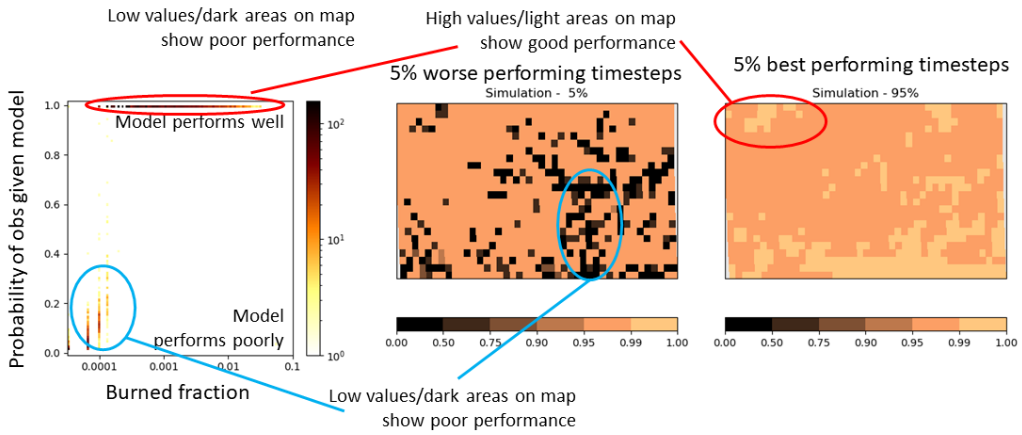

We also determine the percentile of our observations within the model's posterior probability distribution. In an unbiased model, we expect the observation's position to be random. We can start by doing this visually, as shown in the example from **Figure S30**: Observational BA (top left) should generally fall between the two simulation maps (bottom) that span the 5-95 percentile of the model distribution. Taking the cell highlighted in blue for example - the lower model estimate is close to zero and the upper is higher than the observations, indicating a good performance at capturing the observations. Evaluating include parameters representing noise or stochasticity in the system, that is not always included in the main analysis. Given the inherent randomness in fire in our study regions, this does result in very broad BA distributions in the model so a larger difference between the maps showing the BA in the model's tails (“simulation - 5%” and “simulation - 95%”) is to be expected.

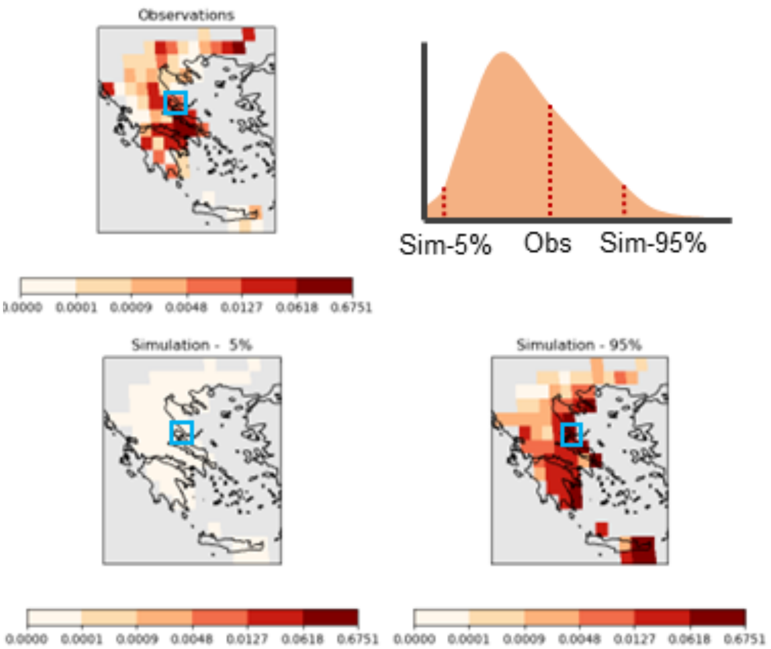

We compare the observations (x-axis) likely range (5-95 percentile) of the model's probability distribution. Similarly to the maps above, if the model captures the uncertainties, the observations should fall within this range - i.e the 1:1 line should fall inside the span of the model, as seen in this example from **Figure S36**. We also calculate the mean position of the observations. This is simply the probability of BA greater than the observation, calculated by integrating equation 7 for BAs in the range $[0, BA]$. For simulations used in attribution, we also build histograms (right, taken from **Figure S39**) of this bias across different percentiles of the observations. This shows us if there is any part of the distribution that has a substantially different bias. In an unbiased model, these observational positions in the framework's probability distribution should average ("Mean Y:" in the histogram) to 0.5. Numbers close to 1 indicate the observations on average tend towards the higher BA in the distribution, and the model generally underestimates BA. This alone does not show if the model performs poorly, and a consistent bias across all parts of the BA distribution indicates correct ranking, though the need for scaling for attribution analysis (see **Supplement Section "Modelling Frameworks > Confire"**).

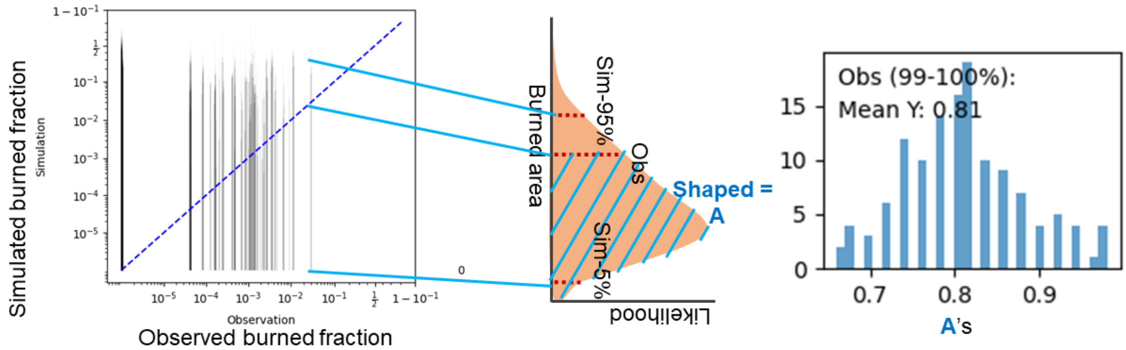

We also map out the mean position of the observations of the times series. Again, in an unbiased model, given enough timestep, this should average out to 0.5 for each gridcell. However, given the small number of timesteps, we map is the observational position in the frameworks posterior tends to be significantly different to 0.5 using a t-test to calculate a p-value for if the mean of the posterior position of the monthly observations for a given grid cell is significantly different from 0.5. Low p-values indicate where the model is biased, which tends to suggest too low or high burning.

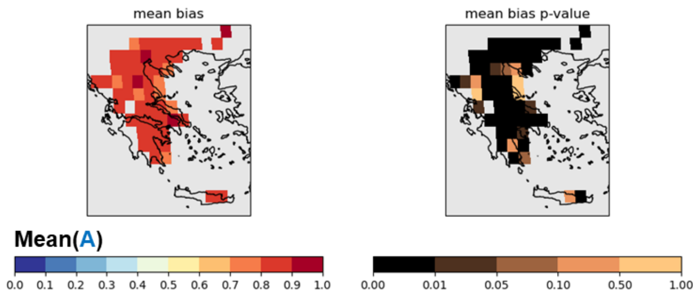

S2.2.1 Drivers of Regional Burned Area Extremes

The model has shown a consistent ability to capture observations within its uncertainty range across all regions, indicating a robust representation of uncertainty. It also demonstrates a high likelihood of aligning with actual observations, indicating strong alignment between model outputs and real-world data. It effectively represents BA anomalies based on the driving variables, demonstrating strong explanatory power across different regions.

However, the model consistently exhibits a low bias in estimating BA across regions, often underestimating the BA, particularly in specific high-burn regions such as deforestation areas in Western Amazonia and patches of high BAin northern Canada. This highlights the common need across regions for better integration of data on human influences and interactions with fire. It may also hint at the need for better representation of none-linearity between drivers and BA.

Canada

Our evaluation indicates that the model's assessment of uncertainty does a reasonable job of capturing the observational range, particularly for high BA. The top row of **Figure S28** demonstrates this - the observed (on the left) falls between the 5-95% range of the model. However, there are patches of high BA that are slightly farther north than in the observations. The model accurately identifies low burning in agricultural regions in southern Saskatchewan and Alberta, and it suggests lower burning in the north while still acknowledging the possibility of some burning.

The probability of observations given the model is very high, especially for medium to high BA ranging from 0.03% to 3% (**Figure S28** left middle row). This demonstrates that the modelling framework does a reasonable job of generating observations within this range..Except for a few locations, even the worst performances tend to show a likelihood of observations given a model of > 0.95. For very high BA, the probability decreases but generally falls within the model's uncertainty range (bottom left), and ranked indicating that the model can effectively identify high burning anomalies. However, it tends to underestimate the increase in BA during such anomalies (i.e in **Figure 10**). Infact, the model tends to be biases towards slightly lower BA in many regions of Canada (bottom middle map), though only significantly so in the South and West of the country (bottom left map). Interestingly, the BA picked up by the driving variables alone also effectively reproduces spatial patterns of BA and regions of high anomalies in 2023, suggesting that the driving variables used are good at explaining the observed patterns in BA.

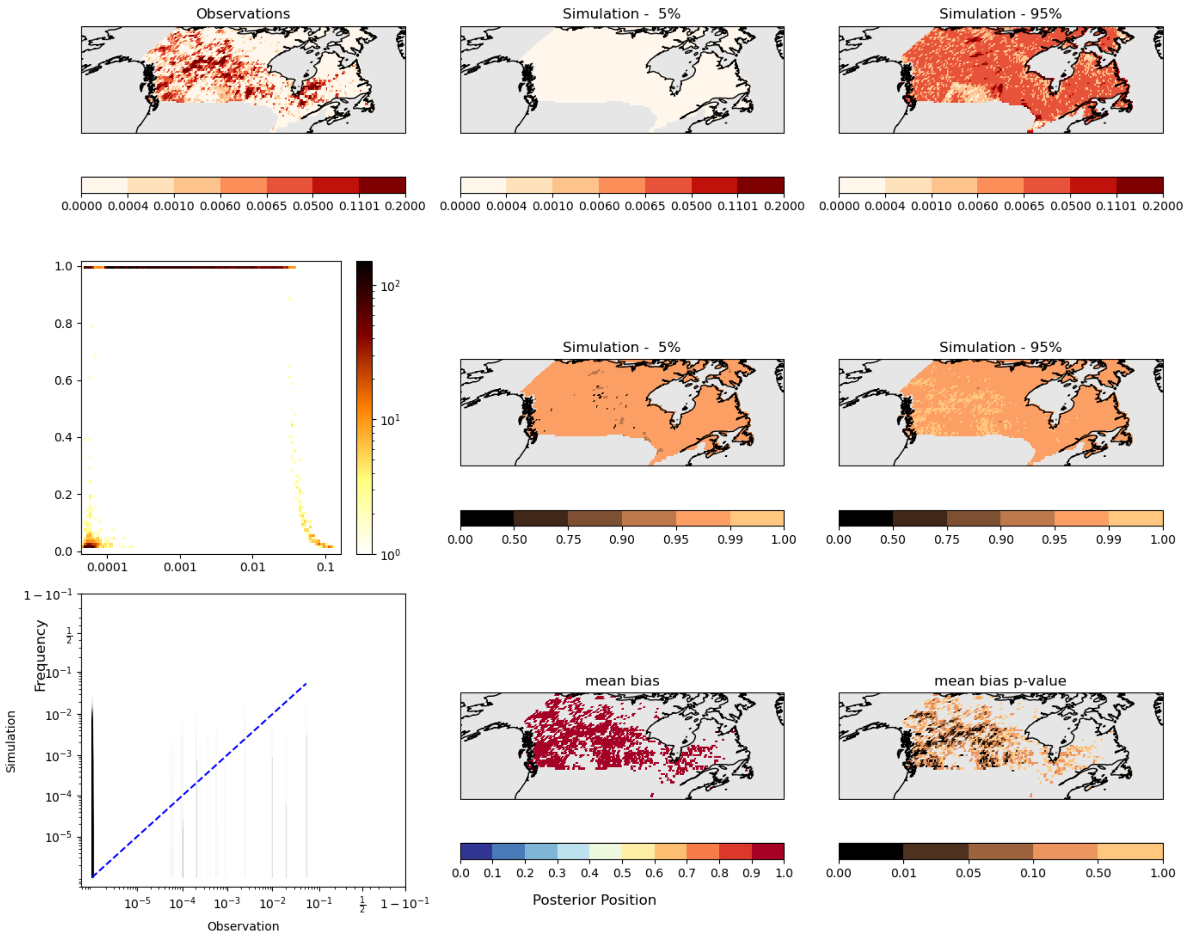

Figure S28: Evaluation plot for driver attribution configuration in **Section 3** over Canada. (top row) observed and simulated BA fraction (%). (Middle row) the likelihood of the out-of-sample observations given the models probability distribution and (bottom row) observations position in the model distribution. See top of this section for interpretation guide.

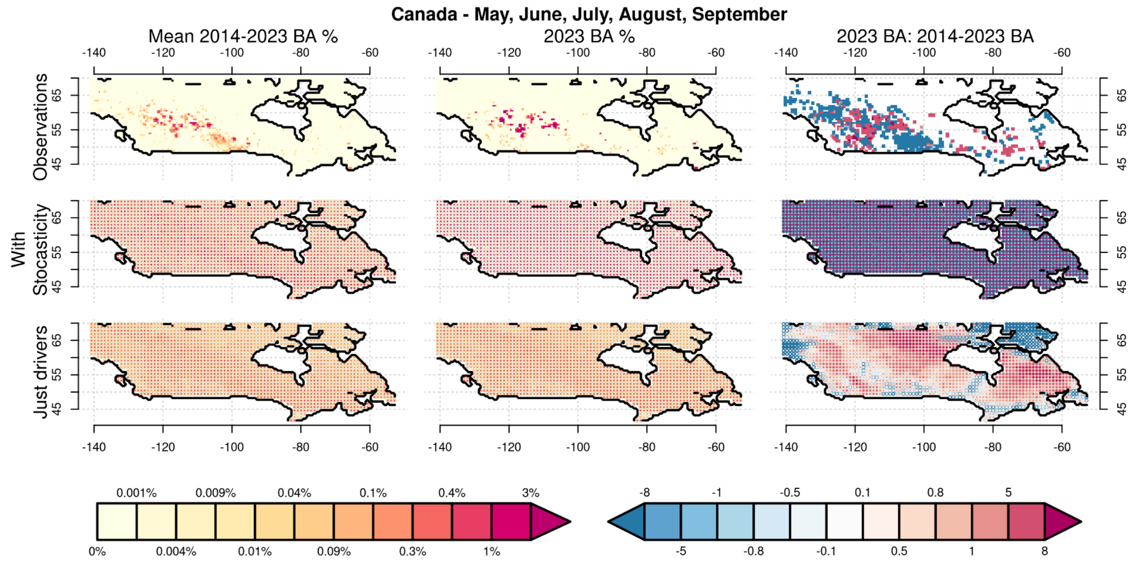

Figure S29: BA % over Canada for May-September for driver attribution configuration in **section 3** over (left) 2014-2023 (middle) 2023 and (right) for 2023 anomaly compared to 2014-2023, expressed as a factor of increase (red) or fractional decrease (blue). The top row is observations, the middle row in ConFire includes stochasticity (equation 7) and the bottom, just considers the influence of drivers (equation 8). For ConFire, the size of the dot in each grid cell shows the likelihood (larger = higher likelihood) of a BA fraction (or BA change) being greater than a given threshold (where the threshold is represented as a coloured dot, see legend at the base). High BA overlap smaller. i.e on the left, a large pale orange dot indicates a high likelihood of annual average BA exceeding 0.1%, with a small dark red dot indicating a small but non-zero likelihood of exceeding 3%

Greece

The model effectively represents uncertainties surrounding observed BA and accurately captures the gradient between low burning in the northwest of Greece and high burning around the southeastern coast. The model's observations show extremely high likelihood across all BA, with only a slight dip to around 0.75 likelihood in a few months in coastal Thessaly. Additionally, there is a consistent pattern of underestimating BA across all areas of Greece, although this is only significant in a few places.

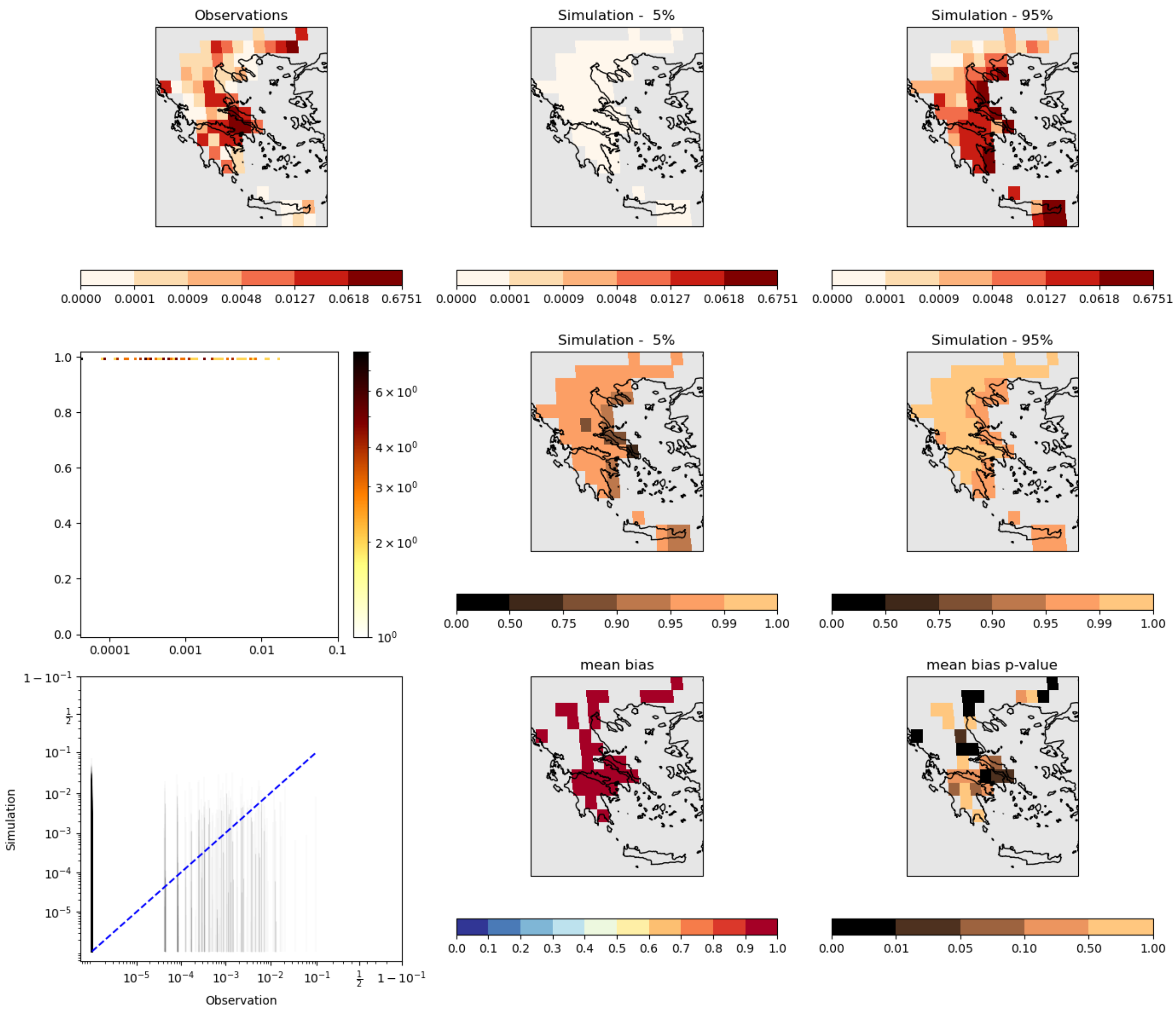

Figure S30: same as **Figure S28** for Greece

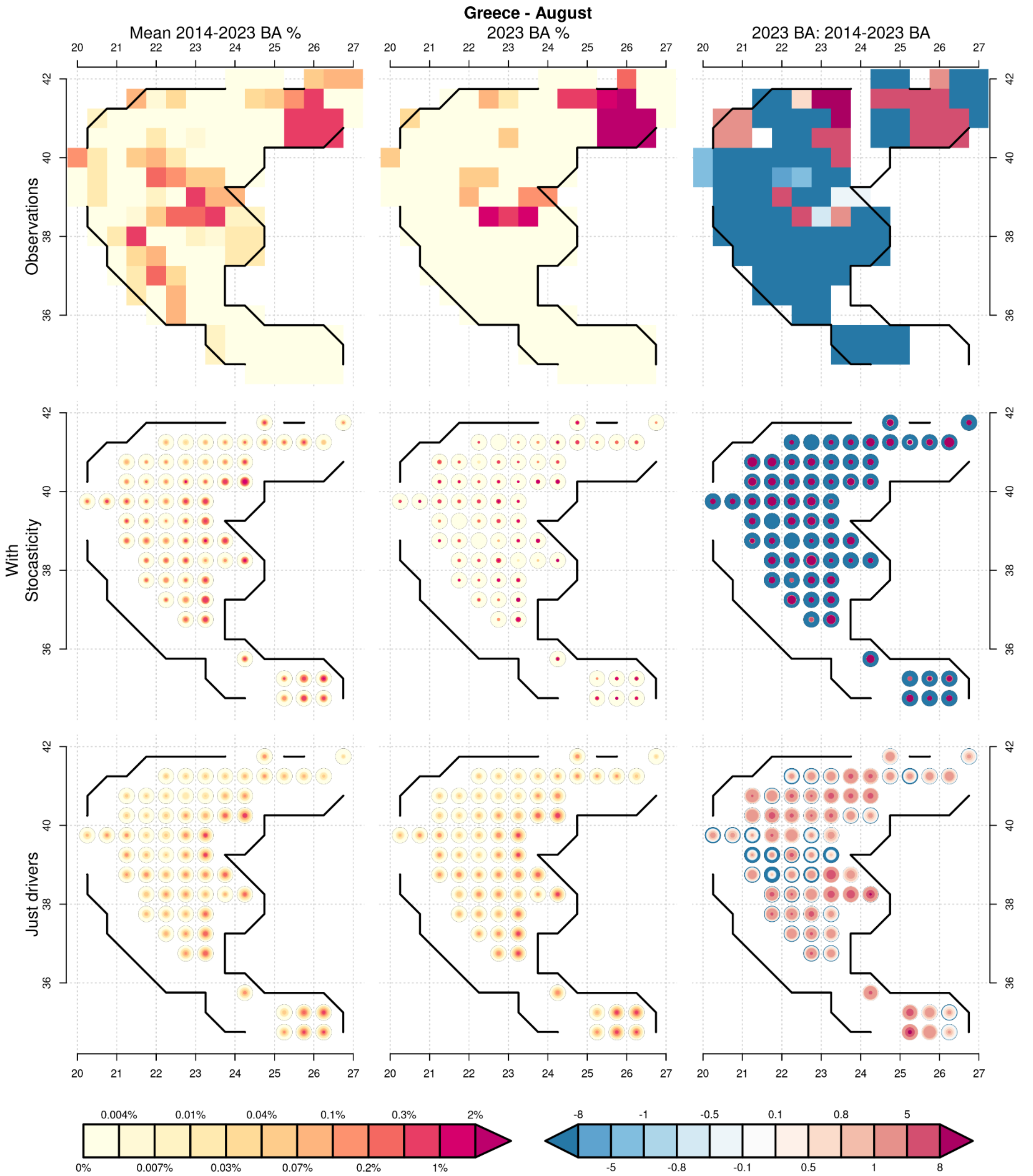

Figure S31: same as **Figure S29** but for Greece in August

Western Amazonia

The model captures observations within its uncertainty range, but it fails to differentiate between high burning in deforestation regions in the south and north of the country. This suggests that vital data on deforestation and its interaction with fire may have been missed. The model is able to generate observations out of its sample, indicated by a high likelihood given observations. However, it does not generate very low BA, particularly in places where high BA are also commonly observed in regions of deforestation. This suggests that the model may fail to capture variations in BA in these human-dominated areas. Similar to the other two regions, the model demonstrated a low bias. However it can accurately capture BA anomalies based solely on the model drivers.

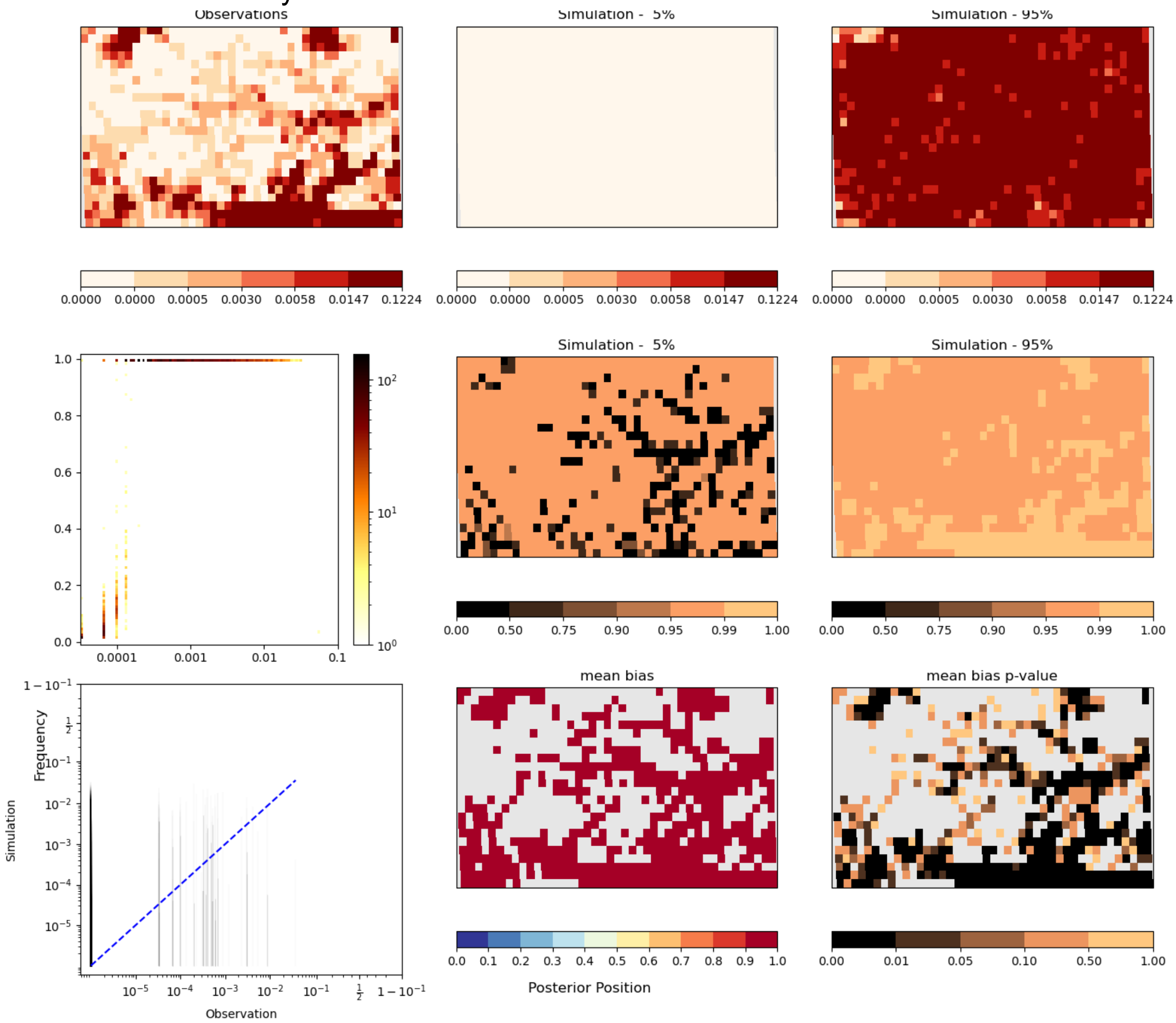

Figure S32: same as **Figure S28** for Western Amazonia

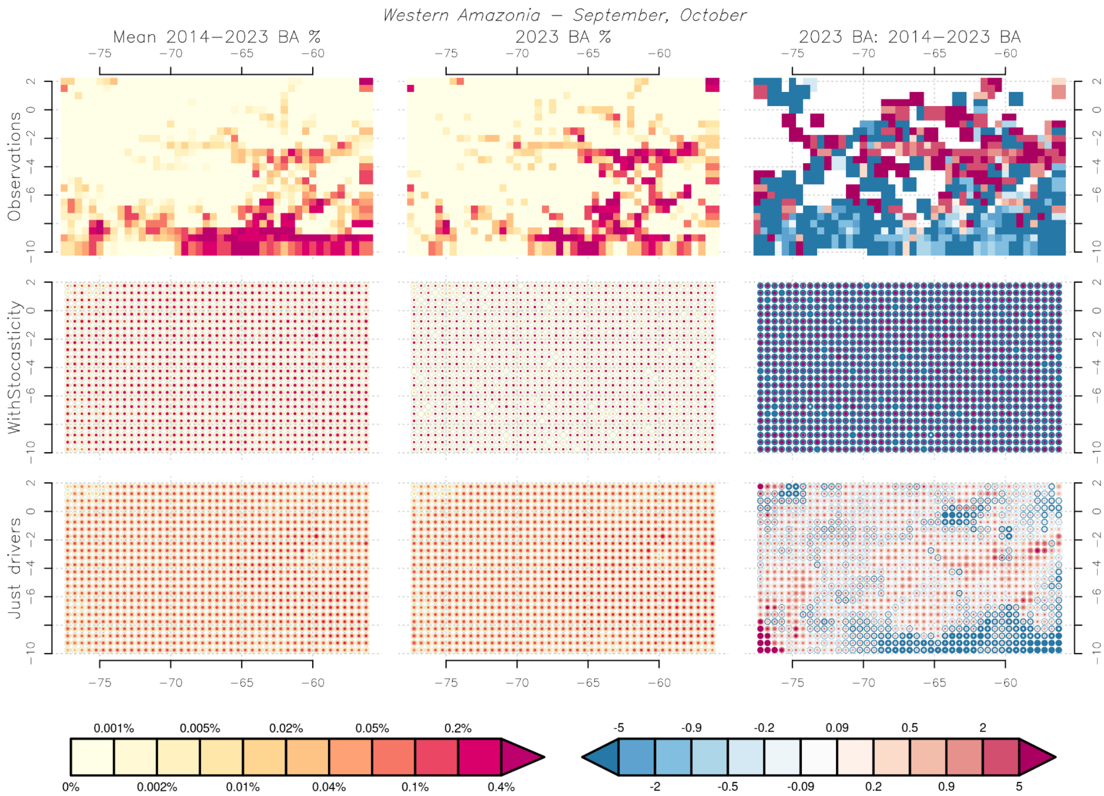

Figure S33: same as **Figure S29** but for Western Amazonia in September and October.

S2.2.2 Change in Likelihood of High Burned Area in 2023 due to Total Climate Forcing and Socioeconomic factors

The framework utilising ISIMIP3a reanalysis data has been found to outperform its near-real-time counterpart in simulating BA. It effectively represents high BA and extremes across all regions. Furthermore, the probability of observations given the model is generally higher in areas with extreme fires or high BA, indicating the model's reliability for attribution analysis.

However, in regions of significant land use change, such as Western Amazonia, the model struggles with reproducing higher BA, indicating a common challenge across regions in capturing detailed land use interactions.

While observations consistently fall within range of the model distribution, the model demonstrates consistent low bias. This simple scaling is suggested to align the model with observations, highlighting a need for calibration to improve accuracy across regions.

Canada

The analysis using isimip reanalysis data shows that the framework performs much better than its near-real-time counterpart in assessing the drivers of BA (**Figure S34**). Although there are still large uncertainty ranges, the highest BA in the distribution closely match the high BA observed. In Canada, the model generally performs slightly worse in generating observations, but it still tends towards a probability of observations given the model of greater than 0.75. However, the model shows that high BA are very likely, indicating that the model is useful in representing extremes - critical for attribution analysis. Overall, the model exhibits less bias than its near real-time version, with observations falling on average around 0.6-0.9 throughout the model's distribution. This consistent pattern across the observed distribution suggests that a simple scaling is required for attribution application (**Figure S35**).

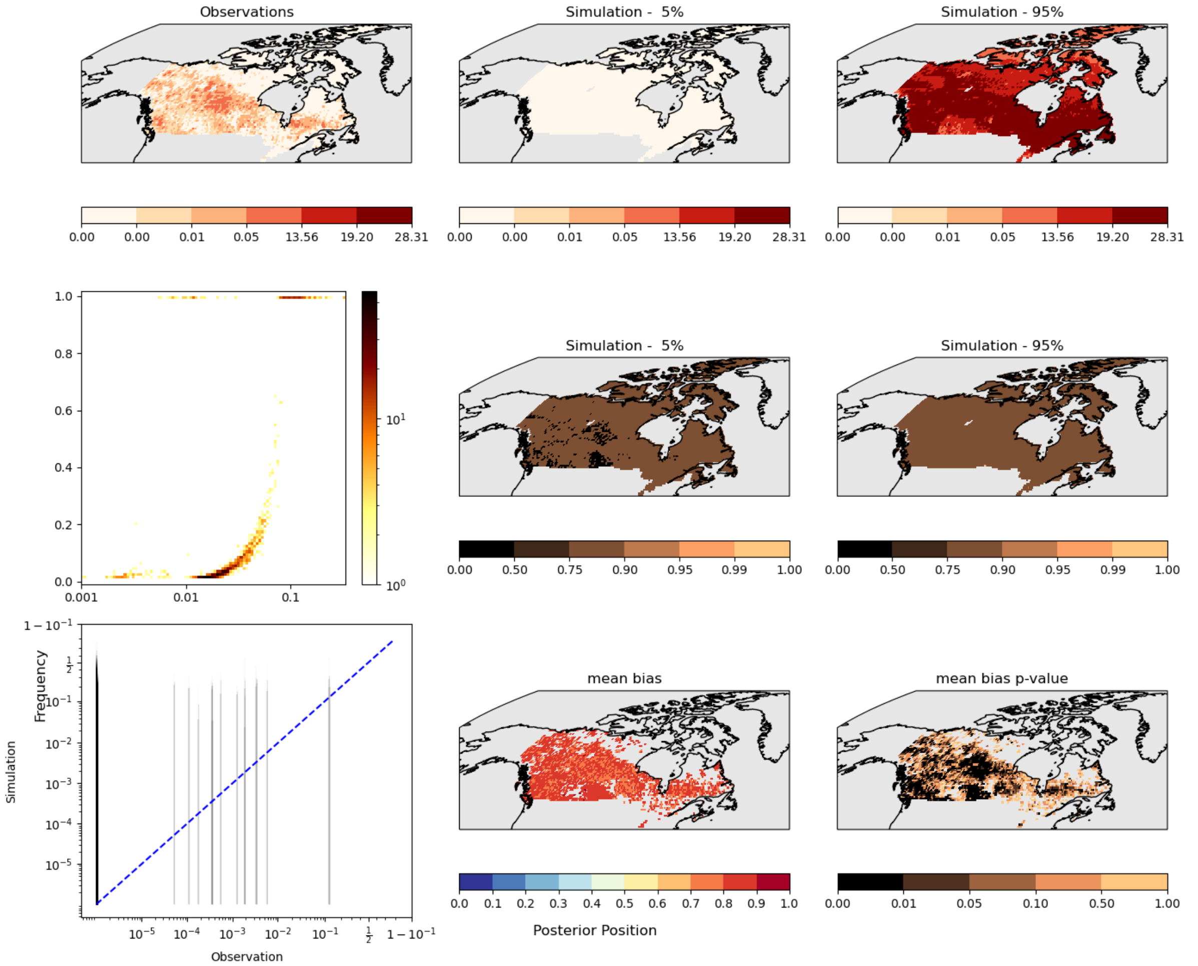

Figure S34: same as **Figure S28** for attribution and future projections configuration used in **section 4** and **section 5**.

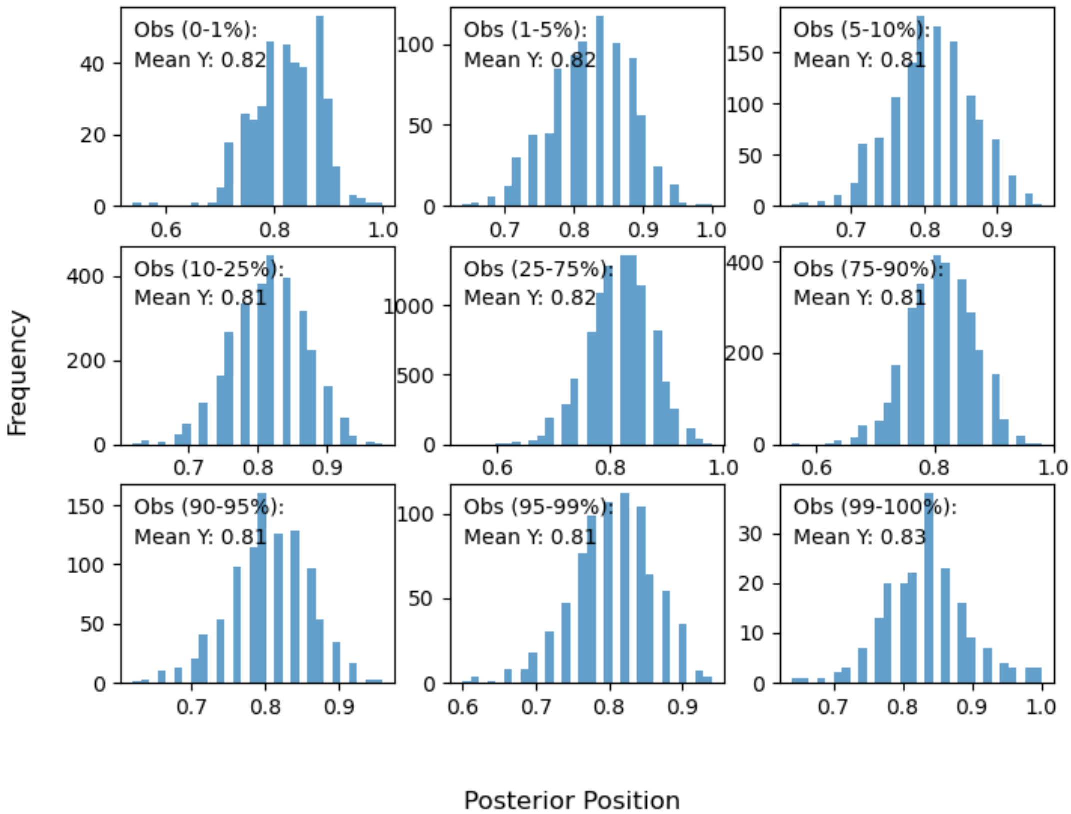

Figure S35: The position of the observed BA in the model's probability distribution over the evaluation period using attribution and future projections configuration from **Section 4** and **Section 5** over Canada. Histograms are for observed percentiles indicated in the top left corner. See start of section for interpretation guide.

Greece

Over the longer evaluation periods, observations tend to be much noisier across Greece than in the near real-time driver analysis (**Figure S36**). However, there is still a noticeable trend towards more burning in the Southeast. This trend is well captured by the model, including the more noisy spatial distribution in the observations. The probability of observing a given model can be quite low, but it tends to be higher in areas where extreme fires were observed and in areas with high burn areas, making it useful for attribution applications. Additionally, while the model is biased low, similar to Canada, this bias is consistent across the observed BA distribution (**Figure S37**).

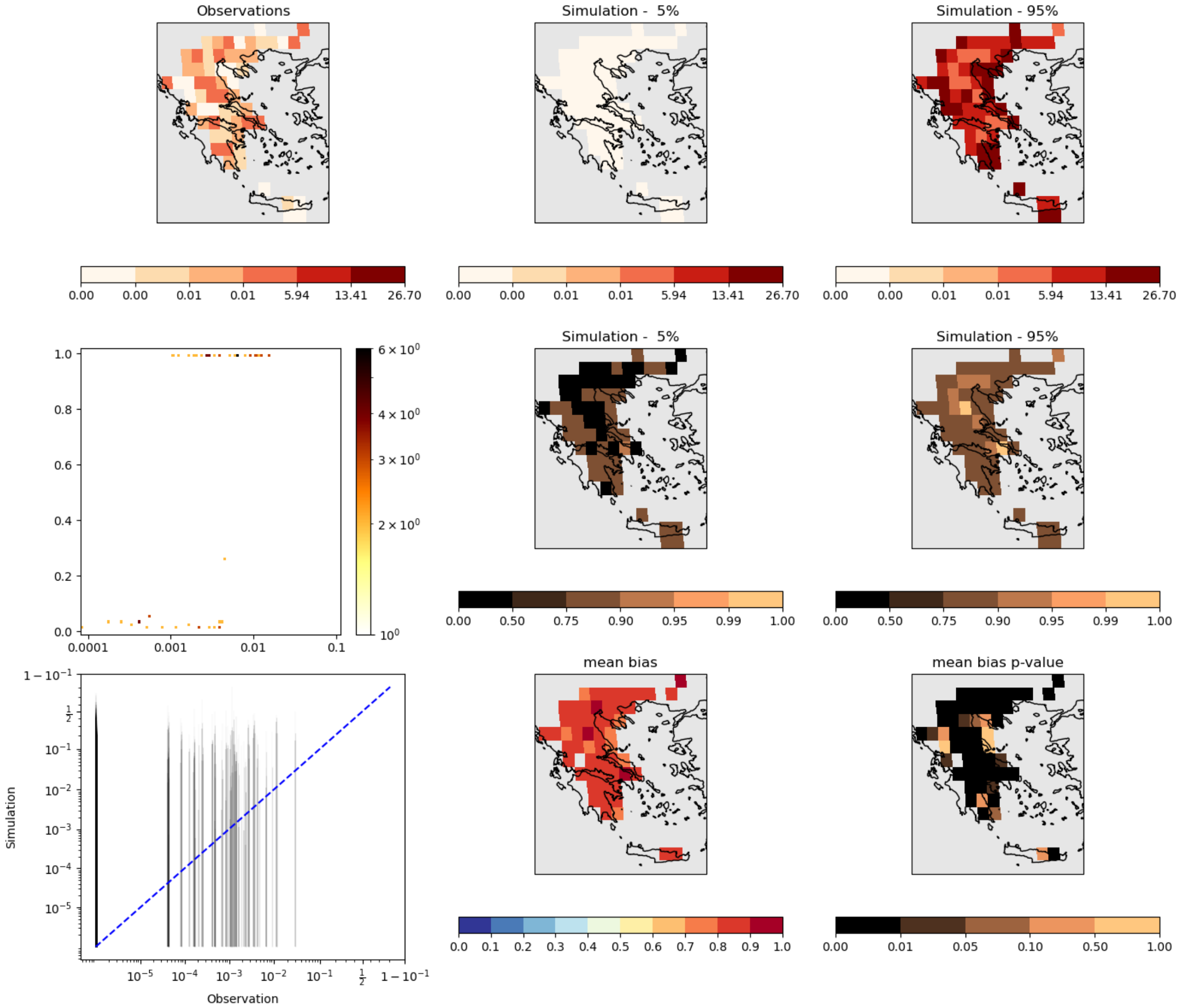

Figure S36: same as **Figure S34** for Greece

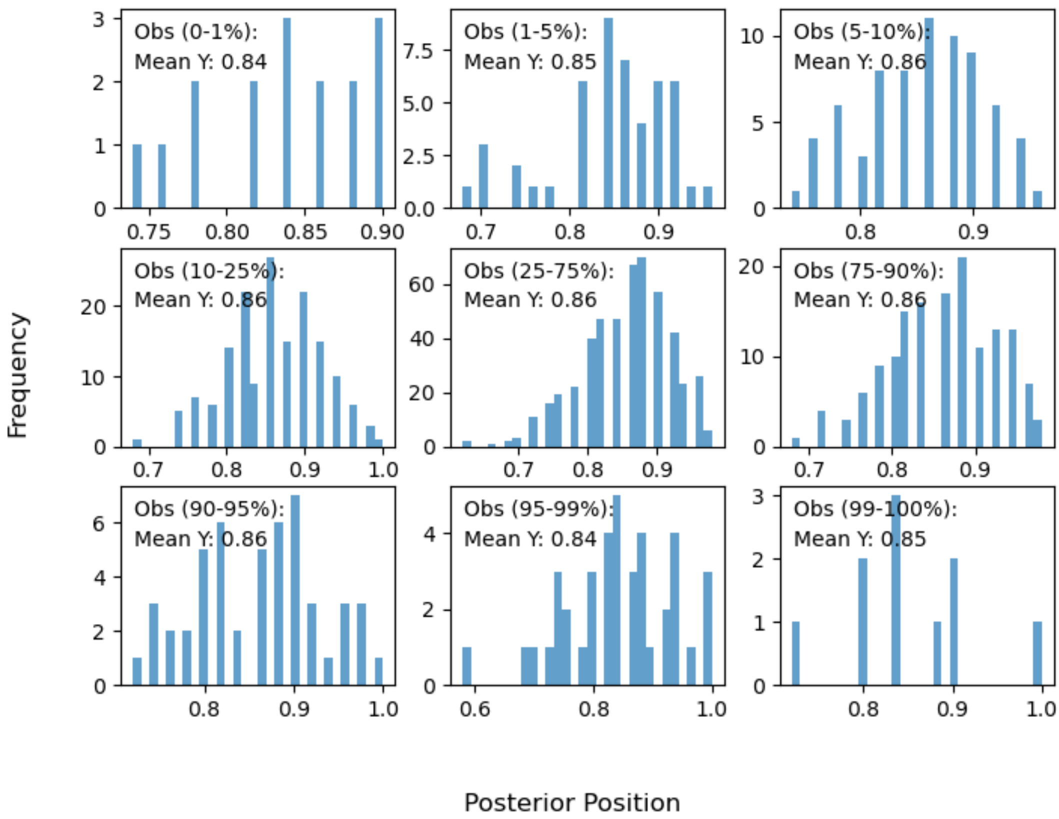

Figure S37: same as **Figure S35** for Greece

Western Amazonia

The framework outperforms its near real time counterpart in simulating higher BA around Manaus, although it still struggles to reproduce higher BA in regions of land use change (**Figure S38**). Observations fall within the model range and, like the other two regions, the observations indicate that the model tends to perform better at generating observed BA at higher levels of burning. Overall, this is the least biased region out of the three, although the model still tends to underestimate BA, with the observations falling at around 0.7-0.8 of the model distribution (**Figure S39**). This pattern is consistent across the distributions .

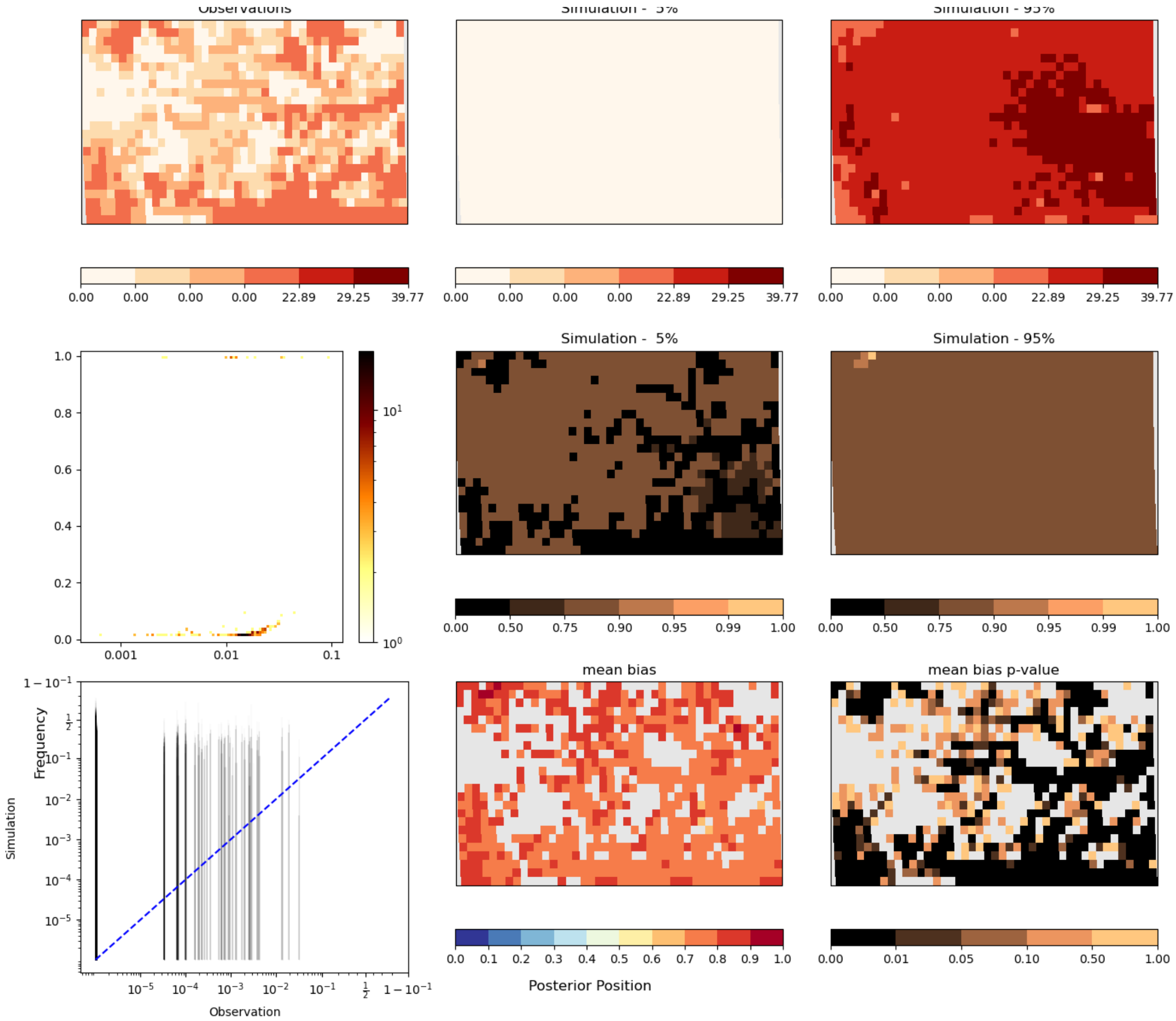

771
772 **Figure S38:** same as **Figure S34** for Western Amazonia.

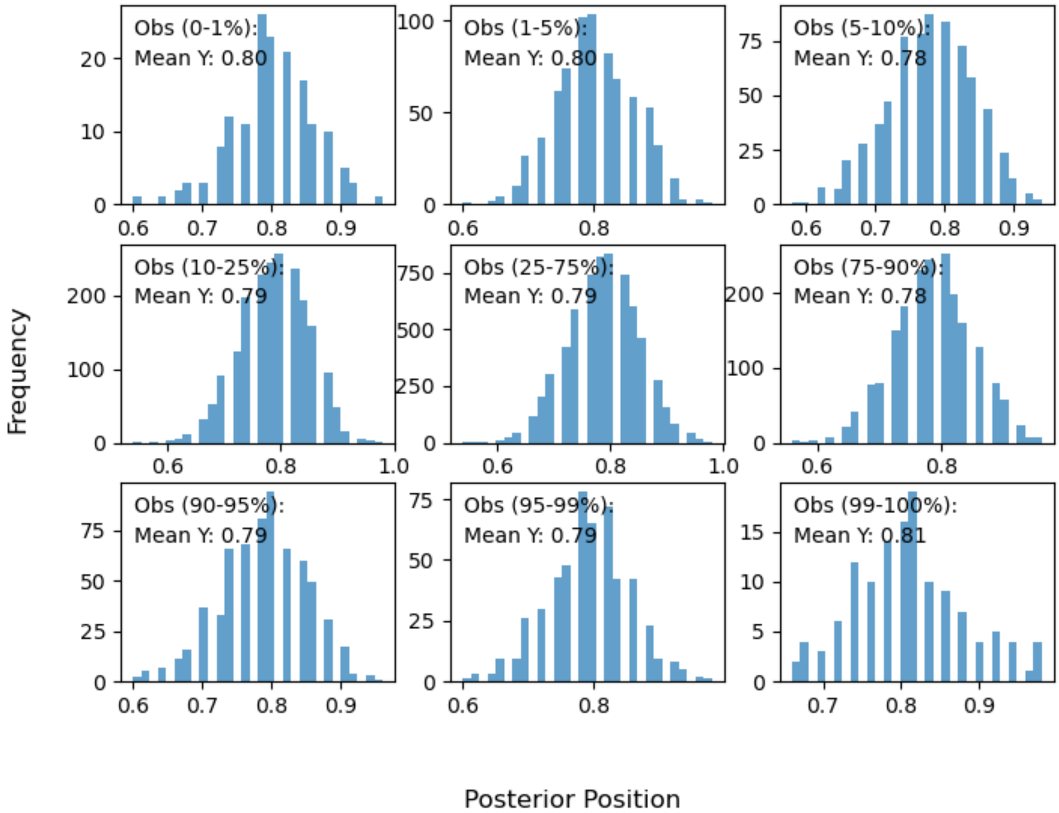

Figure S39: same as **Figure S35** for Western Amazonia

S2.3 Fire Weather attribution

We evaluated each of the component variables used in the FWI against ERA5 reanalysis for the historical period 1960-2013. In each case, HadGEM3 was slightly biased across the timeseries, generally simulating conditions that were too hot and dry in Greece (**Figure S40**). This led to an overall larger bias in the resultant FWI (**Figure S43**). We therefore applied a linear bias-correction to the HadGEM3 ensemble of FWI (see Data and Data Processing). Results before and after the bias-correction is applied are shown below for each region.

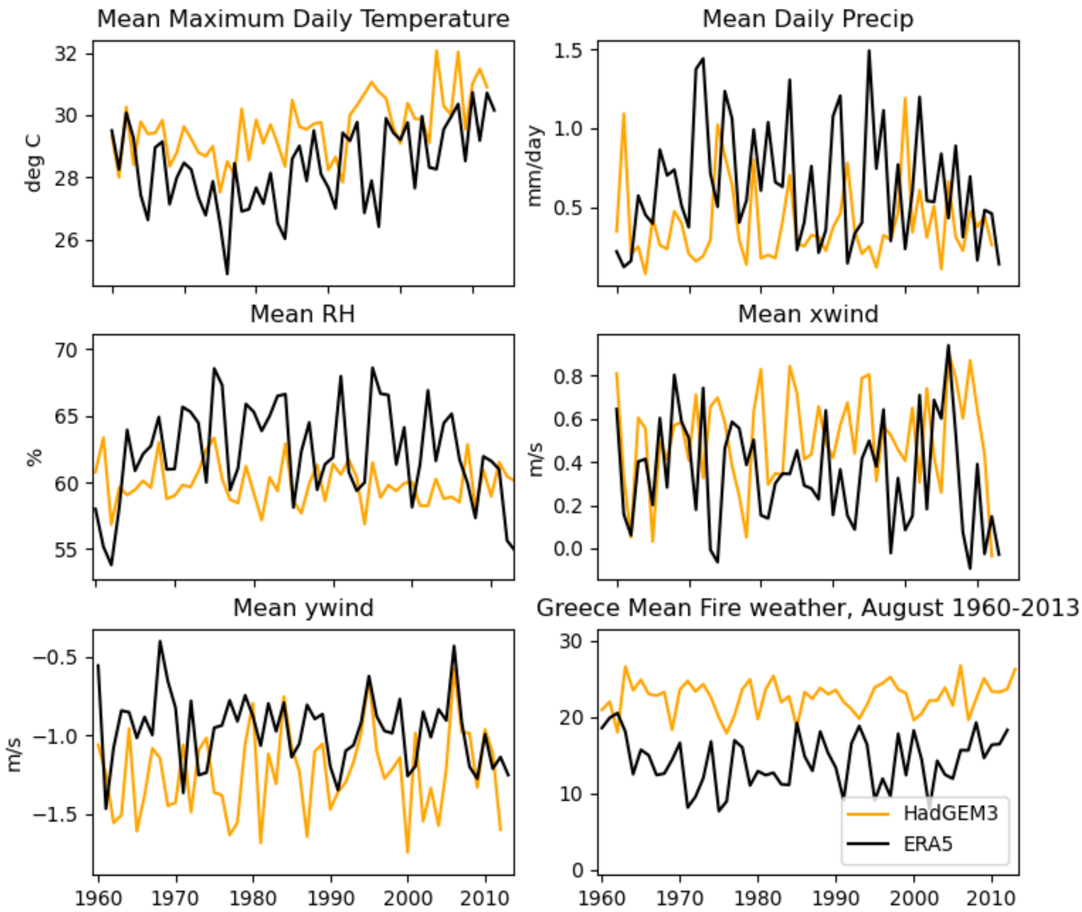

Figure S40: Individual component variables of the FWI compared to ERA5 reanalysis across the historical period (1960-2013), and resultant FWI. Here one member from the HadGEM3 historical ensemble is shown (yellow) against ERA5 (black) for one region (Greece), for illustration

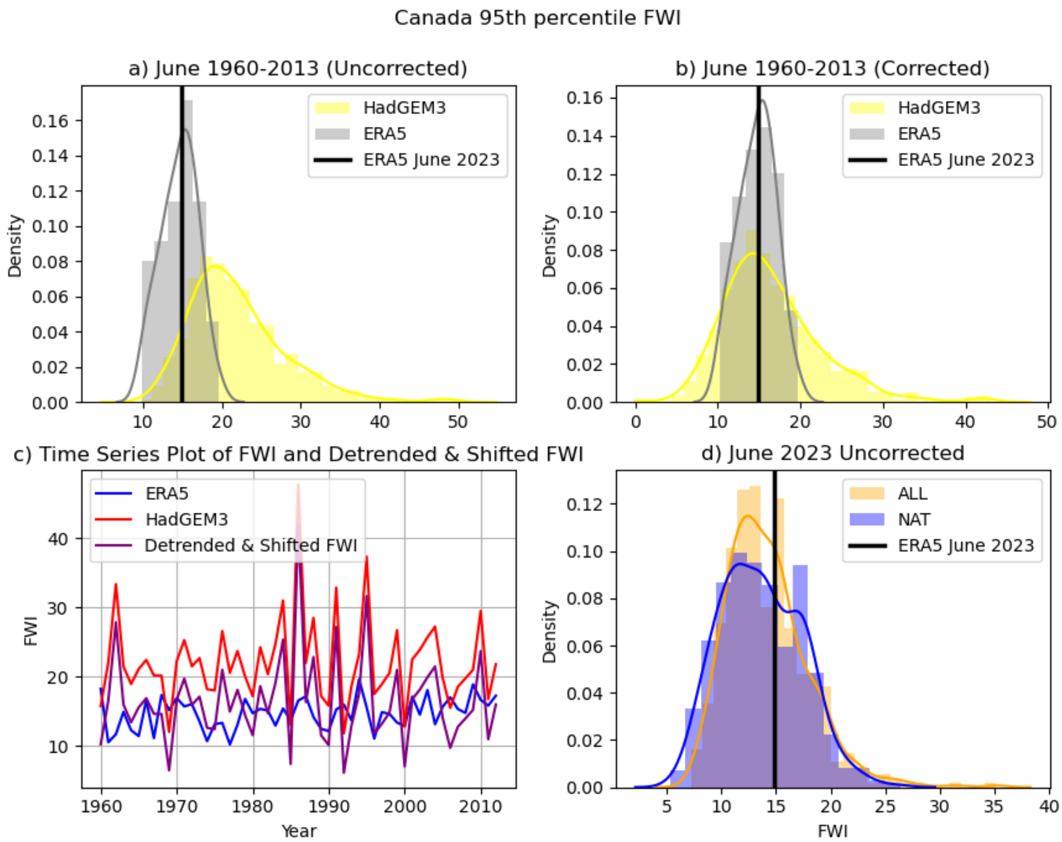

Figure S41: Bias correction for Canada. Historical ensemble of HadGEM3 (yellow) compared to ERA5 (grey) 95th percentile of FWI for the historical period (1960-2013), shown as probability density before correction (a) and after correction (b), and one member shown as a timeseries (c, where HadGEM3 is shown in red, ERA5 in blue and corrected HadGEM3 in purple). HadGEM3 ensemble for 2023 shown before bias-correction (d). ERA5 2023 event shown as black vertical line on all probability density plots.

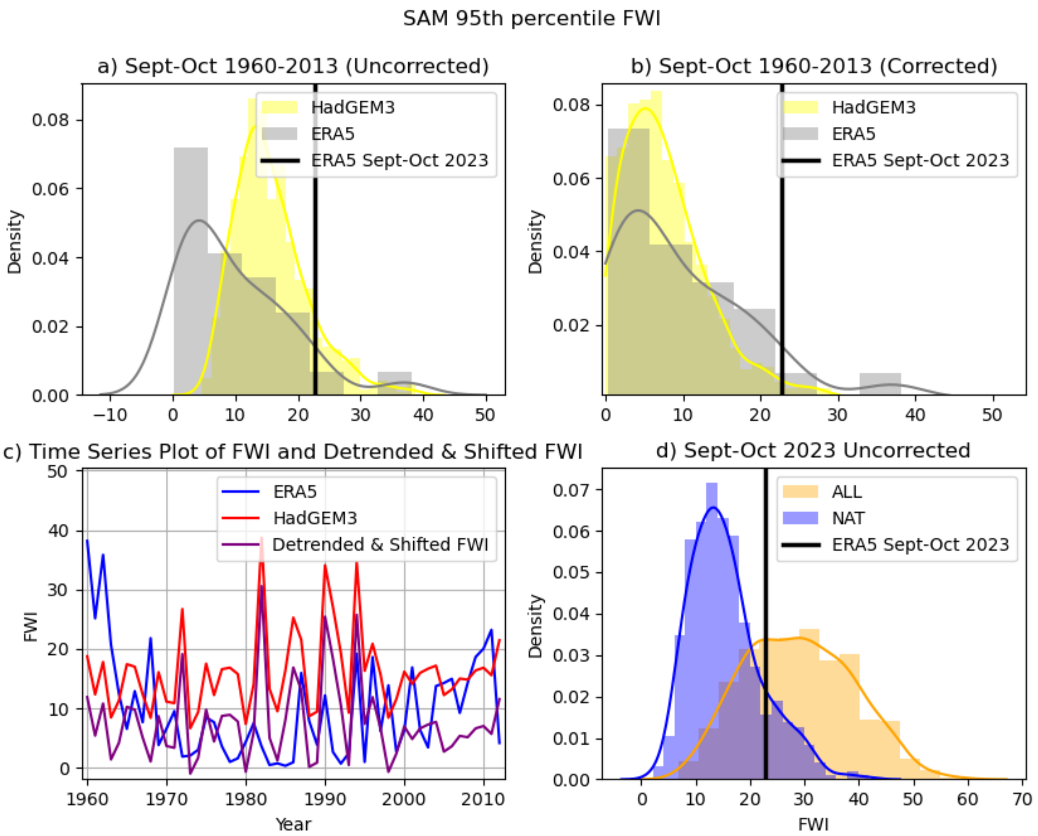

Figure S42: As for **Figure S41**, but for Western Amazonia

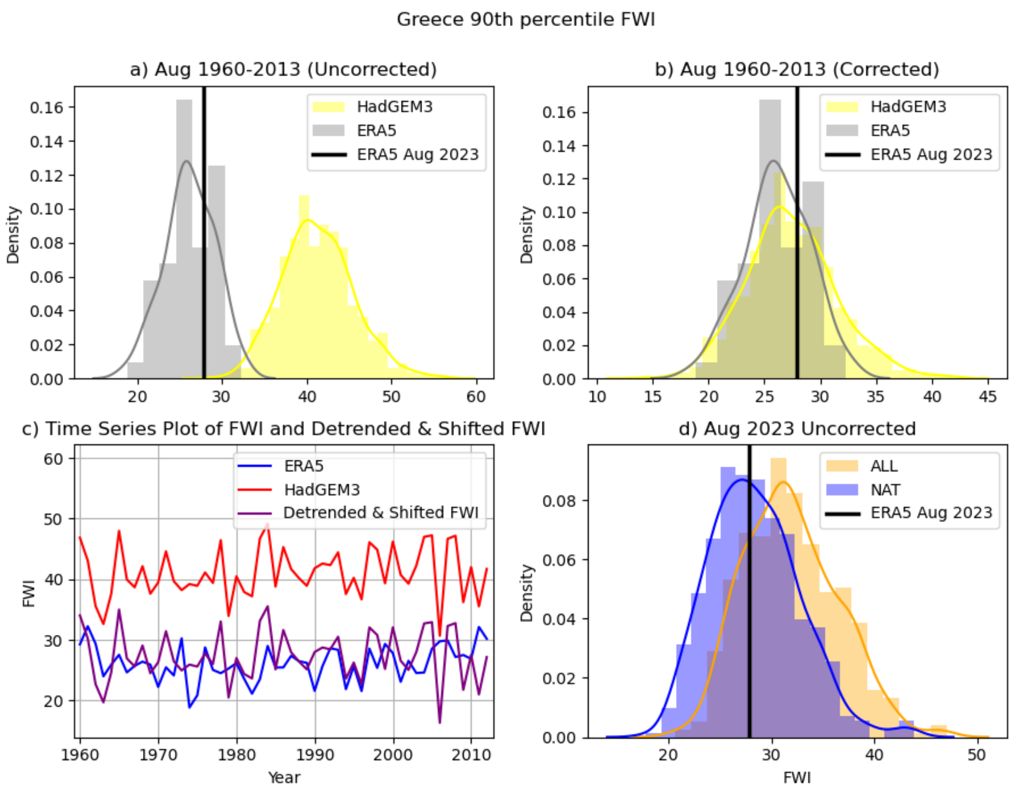

Figure S43: As for **Figure S41**, but for Greece at 90th percentile FWI

Supplementary References

Abril-Pla, O., Andreani, V., Carroll, C., Dong, L., Fonnesbeck, C. J., Kochurov, M., Kumar, R., Lao, J., Luhmann, C. C., Martin, O. A., Osthege, M., Vieira, R., Wiecki, T., and Zinkov, R.: PyMC: a modern, and comprehensive probabilistic programming framework in Python, PeerJ Comput Sci, 9, e1516, https://doi.org/10.7717/peerj-cs.1516, 2023.

Barbosa, M. L. F.: TRACING THE ASHES: UNCOVERING BURNED AREA PATTERNS AND DRIVERS OVER THE BRAZILIAN BIOMES, PhD, Instituto Nacional de Pesquisas Espaciais, 2024.

Burton, C., Betts, R., Cardoso, M., Feldpausch, T. R., Harper, A., Jones, C. D., Kelley, D. I., Robertson, E., and Wiltshire, A.: Representation of fire, land-use change and vegetation dynamics in the Joint UK Land Environment Simulator vn4. 9 (JULES), Geoscientific Model Development, 12, 179–193, 2019.

Burton, C., Betts, R. A., Jones, C. D., Feldpausch, T. R., Cardoso, M., and Anderson, L. O.: El Niño Driven Changes in Global Fire 2015/16, Front Earth Sci. Chin., 8, https://doi.org/10.3389/feart.2020.00199, 2020.

Burton, C., Kelley, D. I., Jones, C. D., and Betts, R. A.: South American fires and their impacts on ecosystems increase with continued emissions, Climate Resilience, 2022.

Burton, C., Lampe, S., Kelley, D. I., Thiery, W., Hantson, S., Christidis, N., Gudmundsson, L., Forrest, M., Burke, E., Chang, J., and Others: Global burned area increasingly explained by climate change, Preprint at https://doi. org/10. 21203/rs, 3, 2023.

Ciavarella, A., Christidis, N., Andrews, M., Groenendijk, M., Rostron, J., Elkington, M., Burke, C., Lott, F. C., and Stott, P. A.: Upgrade of the HadGEM3-A based attribution system to high resolution and a new validation framework for probabilistic event attribution, Weather and Climate Extremes, 20, 9–32, https://doi.org/10.1016/j.wace.2018.03.003, 2018.

Clark, D. B., Mercado, L. M., Sitch, S., Jones, C. D., Gedney, N., Best, M. J., Pryor, M., Rooney, G. G., Essery, R. L. H., Blyth, E., Boucher, O., Harding, R. J., Huntingford, C., and Cox, P. M.: The Joint UK Land Environment Simulator (JULES), model description – Part 2: Carbon fluxes and vegetation dynamics, Geoscientific Model Development, 4, 701–722, https://doi.org/10.5194/gmd-4-701-2011, 2011.

Dimiceli, C. and Others: MOD44B MODIS/Terra Vegetation Continuous Fields Yearly L3 Global 250m SIN Grid V006 (NASA EOSDIS Land Processes DAAC, 2015), 2015.

DiMiceli, C. M., Carroll, M. L., Sohlberg, R. A., Huang, C., Hansen, M. C., and Townshend, J. R. G.: Annual global automated MODIS vegetation continuous fields (MOD44B) at 250 m spatial resolution for data years beginning day 65, 2000? 2010, collection 5 percent tree cover, University of Maryland, College Park, MD, USA, 2017.

Hantson, S., Arneth, A., Harrison, S. P., and Kelley, D. I.: The status and challenge of global fire modelling, 2016.

Hoffman, M. D. and Gelman, A.: The No-U-Turn Sampler: Adaptively Setting Path Lengths in Hamiltonian Monte Carlo, arXiv [stat.CO], arXiv, 1593–1623, https://doi.org/10.5555/2627435.2638586, 2011.

Huang, H., Xue, Y., Li, F., and Liu, Y.: Modeling long-term fire impact on ecosystem characteristics and surface energy using a process-based vegetation–fire model SSiB4/TRIFFID-Fire v1.0, Geosci. Model Dev., https://doi.org/10.5194/gmd-2020-122-

supplement, 2020.

Huang, H., Xue, Y., Liu, Y., Li, F., and Okin, G.: Modeling the short-term fire effects on vegetation dynamics and surface energy in Southern Africa using the improved SSiB4/TRIFFID-Fire model, https://doi.org/10.5194/gmd-2021-116, 2021.

Hugelius, G., Tarnocai, C., Broll, G., Canadell, J. G., Kuhry, P., and Swanson, D. K.: The Northern Circumpolar Soil Carbon Database: spatially distributed datasets of soil coverage and soil carbon storage in the northern permafrost regions, Earth Syst. Sci. Data, 5, 3–13, https://doi.org/10.5194/essd-5-3-2013, 2013.

Ito, A.: Disequilibrium of terrestrial ecosystem CO2 budget caused by disturbance-induced emissions and non-CO2 carbon export flows: a global model assessment, Earth Syst. Dyn., 10, 685–709, https://doi.org/10.5194/esd-10-685-2019, 2019.

Kelley, D. I., Harrison, S. P., Wang, H., and Simard, M.: A comprehensive benchmarking system for evaluating global vegetation models, 2013.

Kelley, D. I., Bistinas, I., Whitley, R., and Burton, C.: How contemporary bioclimatic and human controls change global fire regimes, Nat. Clim. Chang., 2019.

Kelley, D. I., Burton, C., Huntingford, C., and Brown, M. A. J.: Low meteorological influence found in 2019 Amazonia fires, 2021.

Knorr, W., Kaminski, T., Arneth, A., and Weber, U.: Impact of human population density on fire frequency at the global scale, Biogeosciences, 11, 1085–1102, 2014.

Knutti, R., Sedláček, J., Sanderson, B. M., Lorenz, R., Fischer, E. M., and Eyring, V.: A climate model projection weighting scheme accounting for performance and interdependence, Geophys. Res. Lett., 44, 1909–1918, https://doi.org/10.1002/2016gl072012, 2017.

Lange, S.: Trend-preserving bias adjustment and statistical downscaling with ISIMIP3BASD (v1.0), Geosci. Model Dev., https://doi.org/10.5194/GMD-12-3055-2019, 2019.

Lehsten, V., Tansey, K., Balzter, H., Thonicke, K., Spessa, A., Weber, U., Smith, B., and Arneth, A.: Estimating carbon emissions from African wildfires, Biogeosciences, 6, 349–360, https://doi.org/10.5194/bg-6-349-2009, 2009.

Li, F., Zeng, X. D., and Levis, S.: A process-based fire parameterization of intermediate complexity in a Dynamic Global Vegetation Model, Biogeosciences, 9, 2761–2780, https://doi.org/10.5194/bg-9-2761-2012, 2012.

Li, F., Levis, S., and Ward, D. S.: Quantifying the role of fire in the Earth system – Part 1: Improved global fire modeling in the Community Earth System Model (CESM1), Biogeosciences, 10, 2293–2314, https://doi.org/10.5194/bg-10-2293-2013, 2013.

Mangeon, S., Voulgarakis, A., Gilham, R., Harper, A., Sitch, S., and Folberth, G.: INFERNO: a fire and emissions scheme for the UK Met Office's Unified Model, Geosci. Model Dev., 9, 2685–2700, https://doi.org/10.5194/gmd-9-2685-2016, 2016.

Mathison, C., Burke, E., Hartley, A. J., Kelley, D. I., Burton, C., Robertson, E., Gedney, N., Williams, K., Wiltshire, A., Ellis, R. J., Sellar, A. A., and Jones, C. D.: Description and evaluation of the JULES-ES set-up for ISIMIP2b, Geoscientific Model Development, 16, 4249–4264, https://doi.org/10.5194/gmd-16-4249-2023, 2023.

McNorton, J. and Di Giuseppe, F.: A global fuel characteristic model and dataset for wildfire prediction, Biogeosciences, https://doi.org/10.5194/bg-21-279-2024, 2024.

Melton, J., Arora, V., Wisernig-Cojoc, E., Seiler, C., Fortier, M., Chan, E., and Teckentrup, L.: CLASSIC v1.0: the open-source community successor to the Canadian Land Surface Scheme (CLASS) and the Canadian Terrestrial Ecosystem Model (CTEM) – Part 1: Model framework and site-level performance, Geosci. Model Dev., 13, 2825–2850, https://doi.org/10.5194/gmd-2019-329-supplement, 2020.

Mengel, M., Treu, S., Lange, S., and Frieler, K.: ATTRICI v1. 1--counterfactual climate for impact attribution, Geoscientific Model Development, 14, 5269–5284, 2021.

Moritz, M. A., Morais, M. E., Summerell, L. A., Carlson, J. M., and Doyle, J.: Wildfires, complexity, and highly optimized tolerance, Proc. Natl. Acad. Sci. U. S. A., 102, 17912–17917, https://doi.org/10.1073/pnas.0508985102, 2005.

Rabin, S. S., Melton, J. R., and Lasslop, G.: The Fire Modeling Intercomparison Project (FireMIP), phase 1: experimental and analytical protocols with detailed model descriptions, Geoscientific Model, 2017.

Sellar, A. A., Jones, C. G., and Mulcahy, J. P.: UKESM1: Description and evaluation of the UK Earth System Model, in Modeling Earth …, 2019.

Smith, B., Wårlind, D., Arneth, A., Hickler, T., Leadley, P., Siltberg, J., and Zaehle, S.: Implications of incorporating N cycling and N limitations on primary production in an individual-based dynamic vegetation model, Biogeosciences, 11, 2027–2054, https://doi.org/10.5194/bg-11-2027-2014, 2014.

Spuler, F., Wessel, J., Comyn-Platt, E., Varndell, J., and Cagnazzo, C.: ibicus: a new open-source Python package and comprehensive interface for statistical bias adjustment and evaluation in climate modelling (v1.0.1), Geosci. Model Dev., https://doi.org/10.5194/gmd-17-1249-2024, 2024.

Thonicke, K., Venevsky, S., Sitch, S., and Cramer, W.: The role of fire disturbance for global vegetation dynamics: coupling fire into a Dynamic Global Vegetation Model, Glob. Ecol. Biogeogr., 10, 661–677, https://doi.org/10.1046/j.1466-822x.2001.00175.x, 2001.

Thonicke, K., Spessa, A., Prentice, I. C., Harrison, S. P., Dong, L., and Carmona-Moreno, C.: The influence of vegetation, fire spread and fire behaviour on biomass burning and trace gas emissions: results from a process-based model, Biogeosciences, 7, 1991–2011, https://doi.org/10.5194/bg-7-1991-2010, 2010.

UNEP, Popescu, A., Paulson, A. K., Christianson, A. C., Sullivan, A., Tulloch, A., Bilbao, B., Mathison, C., Robinson, C., Burton, C., Ganz, D., Nangoma, D., Saah, D., Armenteras, D., Driscoll, D., Hankins, D. L., Kelley, D. I., Langer, E. R. L., Baker, E., Berenguer, E., Reisen, F., Robinne, F.-N., Galudra, G., Humphrey, G., Safford, H., Baird, I. G., Oliveras, I., Littell, J., Kieft, J., Chew, J., Maclean, K., Wittenberg, L., Anderson, L. O., Gillson, L., Plucinski, M., Moritz, M., Brown, M., Soto, M. C., Flannigan, M., Costello, O., Silva, P. S., Fernandes, P., Moore, P., Jandt, R., Blanchi, R., Libonati, R., Archibald, S., Dunlop, S., McCaffrey, S., Page, S., Gonzãƒâ¡lez, T. D. T., Sokchea, T., and Charlton, V.: Spreading like Wildfire: The Rising Threat of Extraordinary Landscape Fires, edited by: Sullivan, A., Kurvits, T., and E., B., United Nations Environment Programme and GRID-Arendal., 2022.

Yue, C., Ciais, P., Cadule, P., Thonicke, K., Archibald, S., Poulter, B., Hao, W., Hantson, S., Mouillot, F., Friedlingstein, P., Maignan, F., and Viovy, N.: Modelling the role of fires in the terrestrial carbon balance by incorporating SPITFIRE into the global vegetation model ORCHIDEE – Part 1: simulating historical global burned area and fire regimes, Geoscientific

Model Development, 7, 2747–2767, https://doi.org/10.5194/GMD-7-2747-2014, 2014.

Yue, C., Cadule, P., and Van Leeuwen, T. T.: Modelling the role of fires in the terrestrial carbon balance by incorporating SPITFIRE into the global vegetation model ORCHIDEE--Part 2: Carbon emissions and the role of fires in the global carbon balance, Geoscientific Model Development, 8, 1321–1338, 2015.

European Commission EU Science Hub: Wildfires in the Mediterranean: EFFIS data reveal extent this summer, available at: https://joint-research-centre.ec.europa.eu/jrc-news-and-updates/wildfires-mediterranean-effis-data-reveal-extent-summer-2023-09-08_en, last access:, 2023.

Schroeder, W., Oliva, P., Giglio, L., and Csiszar, I. A.: The New VIIRS 375 m active fire detection data product: Algorithm description and initial assessment, Remote Sensing of Environment, 143, 85–96, https://doi.org/10.1016/j.rse.2013.12.008, 2014.

Xanthopoulos, G., Zevgoli, E., Kaoukis, K., and Athanasiou, M.: Greece - Lessons not learned, available at: https://issuu.com/wildfiremagazine-iawf/docs/wildfire_magazine_q4_2023_-_web, last access:, Wildfire, 2023, 2024.